Impact of Entropy on Black Hole Astrophysics

Thesis by
Siyuan Chen

In Partial Fulfillment of the Requirements for the
Degree of
Honors Bachelor of Science in Physics

VANDERBILT UNIVERSITY
Nashville, Tennessee

2024
Defended 18 April

Siyuan Chen
ORCID: xxxxx

ACKNOWLEDGEMENTS

I would like to express my greatest gratitude to Professor Karan Jani for the consistent mentorship and guidance throughout my undergraduate career, both in research and life. Thank you for all your inspiration, patience, and wisdom that transformed the daunting into the doable, which shaped me into a better person I never expected before.

I am grateful for the participation of my honor examination committee members – Professor Runnoe, Professor Holley-Bockelmann, and Professor Johns. Thank you for becoming my first audience to hear about my cherishment to the cosmos.

A special thank to Patrick Hu, who provided the initial study design and led me from scratch. Thank you to graduate student Krystal Ruiz-Rocha for answering my countless perplexities and always being a role model that motivates me.

Thank you to the Office of Experiential Learning & Immersion Vanderbilt and the LittleJohn Family for funding this research. And thank you to the Department of Physics & Astronomy for providing the opportunity to write this thesis.

This material and data is based upon work supported by NSF's LIGO Laboratory which is a major facility fully funded by the National Science Foundation. I am grateful to every member of this LIGO family, where I truly find senses of belonging in the broad spectrum of physics and astronomy.

Lastly, thank you to my parents for your unwavering love and unconditional support on my way to pursue this universe. You give the first encouragement and guidance in my spacetime, and your devotion illuminates every chapter of my life.

ABSTRACT

As an irreversible natural process, mergers between two black holes will increase the entropy of the universe. By imposing thermodynamical constraints derived from general relativity and quasi-circular hypothesis, we showcase `BRAHMA` – a novel framework to infer the properties and astrophysical implications of binary black hole mergers in LIGO-Virgo-KAGRA (LVK). We apply the framework as an IMR (inspiral-merger-ringdown) consistency test to 10 heaviest binary black hole merger events reported by LVK Collaboration and perform a systematic investigation on the consistency between phenomenological waveform and ringdown models (analysis data available on Zenodo). In doing so, we obtain astrophysical insights into the origins of black holes for GW190521 and GW191109, two of the heaviest confirmed merger events. We also show the high consistency of the NRSur7dq4 waveform and Kerr_{221} ringdown model, providing insights into the timing of the ringdown stage. For events without QNM measurements due to low SNR of ringdown, we use the post-merger conditions inferred from phenomenological waveforms to compute the $\mathcal{I}_{\mathrm{BBH}}$ (Merger Entropy Index: measures the efficiency of entropy transfer during BBH merger) distribution across all GW events. $\mathcal{I}_{\mathrm{BBH}}$ shows high differentiability in formation channels, which can be used as a tool to classify compact binary populations. Therefore, we employ $\mathcal{I}_{\mathrm{BBH}}$ to identify compact objects in the lower mass gap ($2.5 \backsim 5M_{\odot}$), including the newest discovery GW230529 in the 4th observing run.

TABLE OF CONTENTS

LIST OF ILLUSTRATIONS

LIST OF TABLES

Chapter 1

INTRODUCTION & BACKGROUND

1.1 Gravitational Wave

Gravitational waves (GW) are "ripples" in spacetime predicted by Albert Einstein's general relativity in 1916 (B. P. Abbott et al., 2016b). GW events are caused by mergers between compact objects, including black holes and neutron stars. We can classify such events into three categories – binary black hole (BBH) mergers (B. P. Abbott et al., 2016b), neutron star-black hole (NS-BH) mergers (R. Abbott et al., 2021a), and binary neutron star (BNS) coalescence (B. P. Abbott et al., 2019). GW signals reflect the three stages of the merger/coalescence events – inspiral, merger, and ringdown (Pan et al., 2014). The full gravitational wavelet is shown in Fig. 1.1. During the inspiral stage (blue sector), two compact objects orbit around each other, producing a sinusoidal signal. The signal peaks when two compact objects collide and merge (orange sector). After the merger, the remnant object will be highly unstable and distorted, so it will radiate GWs when transferring to the equilibrium state. In this process, the post-merger object will ring like a "bell" (green sector). The noise of the "bell" in compact object coalescence will be oscillation in the spacetime, which is reflected in GWs.

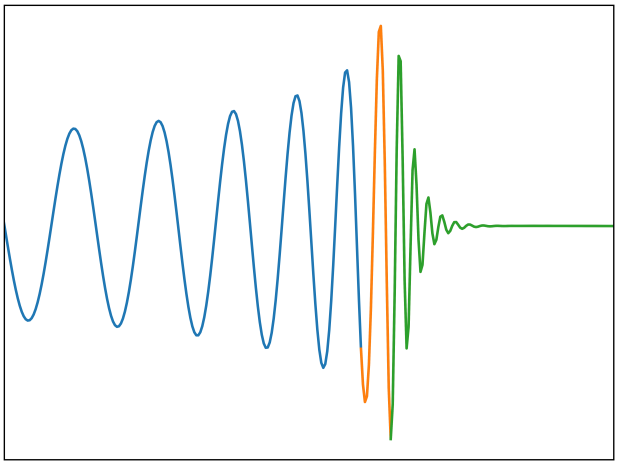

Figure 1.1: GW wavelet generated by PyCBC

Laser Interferometer Gravitational-Wave Observatory (LIGO) is a Michelson interferometer that measures GWs. The two 4km arms of the detector are orthogonal

to each other, forming a L-shape. Lasers travel through the arms and are reflected by the test masses (mirrors) in the end of each arm. GWs will alter the arm length and change the phase difference of the two light beams, which enable us to detect the signal. With the enhancements of the detector, LIGO eventually measured the first GW signal in 2015 (B. P. Abbott et al., 2016b), which opened the new field of gravitational-wave astronomy. GW data is organized in the Gravitational-Wave Transient Catalogs (GWTC). For this study, we will mainly use results from GWTC-2 from the first half (L. S. Collaboration and V. Collaboration, 2021) and GWTC-3 from the second half of the third LIGO observation run (L. S. Collaboration, V. Collaboration, and K. Collaboration, 2023).

Depending on different fitting techniques, the wavelet can deviate slightly, corresponding to different waveform models. In LIGO, there are three waveform families: EOBNR, Phenom, and NR surrogate. The EOBNR family represents Effctive-One-Body Numerical Relativity, which combines the Effective-One-Body (EOB) formalism and Numerical Relativity (NR) simulations. The analytical fit is based on post-Newtonian and BH perturbation theory, with NR to calibrate the waveform. The Phenom family represents phenomenological fits from a frequency-domain description that combines the inspiral information from EOB formalism and merger information from numerical relativity (R. Abbott et al., 2020a). On the other hand, NR surrogate completely depends on the NR waveform (Varma, Field, et al., 2019). These three families can have different treatments to parameters including higher multipoles, which account for the difference in observation.

1.2 Entropy

In the nineteenth century, Rudolf Clausius first established the concept of entropy in thermodynamics. After years of continued research, Ludwig Boltzmann refined the idea of entropy as the measure of disorder (Popovic, 2017). Clausius also discovered the second law of thermodynamics ("entropy law") – irreversible processes such as the merger between two black holes (B. P. Abbott et al., 2016a) would increase the entropy of the system, which is the universe (Bekenstein, 1973). After Einstein predicted the existence of black holes together with his relativity theorem, scientists started to investigate the thermodynamics of black holes in the twentieth century. Unexpectedly, they noticed some incompatibilities between the conventional laws of thermodynamics and black hole mechanics (Bardeen, Carter, and Hawking, 1973).

The "No-hair theorem" is the key to black hole mechanics (Isi et al., 2019), suggest-

ing that black holes are characterized by three parameters - mass, charge, and spin (angular momentum). All other information, including entropy, would vanish, so observers outside the event horizon could never observe other parameters of black holes. This theorem disagrees with the conventional second law of thermodynamics. Consider the case when an object with comparative entropy dropped into a black hole, the entropy of that object would “disappear" inside the event horizon. Consequently, combining this object and the black hole would result in a decrease in the total entropy of the system, which disobeyed the “entropy law.” This meant that when an object with comparative entropy dropped into a black hole, the entropy of that object would “disappear." Consequently, combining two objects (the object with entropy and the black hole) would result in a decrease in the total entropy of the system, which disobeyed the second law of thermodynamics. Such conflicts urge scientists to adjust the law of thermodynamics by incorporating Hawking radiation (Hawking, 1971). The corrected second law of thermodynamics for black holes suggested that the entropy of a black hole could never decrease, so BBH mergers will always increase the entropy of the universe (Bardeen, Carter, and Hawking, 1973).

According to the first law of black hole mechanics, the entropy of a black hole is correlated to the surface area of its event horizon, which is given by the Bekenstein-Hawking Formula (Bekenstein, 1973):

$$S_{BH} = \frac{A}{4l_p^2}$$

where A is the surface area of the event horizon, and l_p is the Planck length. When two black holes merge, the surface area increases, thus increasing the entropy according to the formula. Meanwhile, two black holes can never be separated after the merger, so BBH merger is an irreversible process, which was another indication of entropy increase.

In this study, we connect entropy with gravitational waves by rewriting the Bekenstein-Hawking Formula in terms of mass and spin for Kerr black holes (Bekenstein, 1973), which are two parameters that characterize black holes according to the no-hair theorem. Mass and spin are also directly measured by LIGO, so we can calculate the entropy of black holes from GW data (Hu et al., 2021).

$$S = \frac{Ac^2}{4G\hbar^2} = \frac{2\pi G}{\hbar c} m^2 (1 + \sqrt{1 - \chi^2})$$

Here, m is the mass of the black hole, and χ is the spin of the black hole (some paper denotes spin as a). With information from GWs, we could calculate the entropy of the two pre-merger black holes ($m_{1,2}$, $|\chi_{1,2}|, S_{1,2}$) and the remnant post-merger black hole (m_f, $|\chi_f|, S_f$).

1.3 Ringdown Models

The ringdown stage shows a superposition of exponentially damped sinusoidal signal called quasinormal modes (QNM) (Berti, Cardoso, and Starinets, 2009). Ringdown modes are characterized by their unique frequencies and damping times:

$$\omega = 2\pi f + \frac{i}{\tau}$$

where f is the oscillation frequency in spacetime and τ is the damping time. The QNM frequency contains both a real part and an imaginary part. In QNMs, this frequency ω is indexed with three parameters: polar ℓ ($\ell \geq 2$), azimuthal m ($-\ell \leq m \leq \ell$), and overtone n ($n \geq 0$) (Finch and Moore, 2021). For Kerr black holes detected by LIGO, the ringdown modes are denoted as $\text{Kerr}_{\ell mn}$. LIGO uses $_{\text{PY}}$Ring analysis (Carullo, Del Pozzo, and Veitch, 2023) to fit the ringdown stage, which is a time-domain approach (Isi et al., 2019; R. Abbott et al., 2021b). There are three templates Kerr_{220} (fundamental modes), Kerr_{221}(fundamental modes + first overtone), and Kerr_{HM} (higher moments with $\ell \leq 4$) (R. Abbott et al., 2021c). The dominant QNM of LIGO is expected to be Kerr_{220} (Abhirup Ghosh, Brito, and Buonanno, 2021) because GW strain is dominated by $\ell = |m| = 2$. Meanwhile, the overtone can decay very fast, so the dominant overtone in the ringdown stage is the fundamental n = 0, especially later in the wavelet (Finch and Moore, 2021).

The remnant black hole after the merger also follows the no-hair theorem (Isi et al., 2019), which means that the final black hole is characterized by the final mass (m_f) and final spin (χ_f). The frequency and damping time completely depend on m_f and χ_f, enabling us to infer the post-merger parameters from QNMs.

However, not all GW events detected by LIGO have QNM measurements that gives robust post-merger parameters, which we consider as an independent ringdown analysis in the later sections. The ringdown phase has a low signal-to-noise ratio (SNR) after the peak merger stage (Isi et al., 2019). For example in Fig. 1.2, the ringdown stage (when characteristic strain dramatically drops) is mostly under the LIGO noise curve, making it difficult to obtain a QNM measurement. In this case,

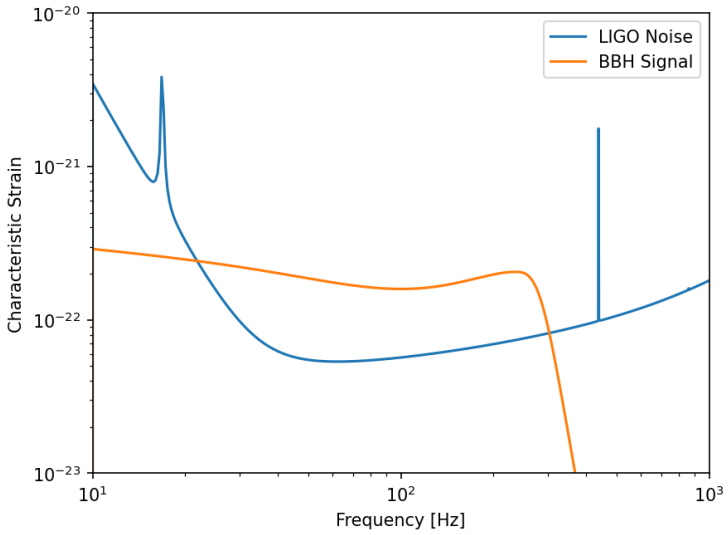

Figure 1.2: LIGO noise curve and the BBH merger signal

we can still use the post-merger conditions inferred from the phenomenological waveform (Ma et al., 2022).

1.4 Astrophysical Mass Gap

Both from observational data such as X-ray binaries (XRB) and stellar evolution theories, there exist some astrophysical mass gaps where there is a dearth of black holes. GW detection from LIGO challenges the existence of these mass gaps, which we will investigate in this project.

Pair-Instability Supernovae Mass Gap

Stellar evolution and nucleosynthesis theory predicts a mass gap between [50, 130]$M_{\odot}$, where black holes should not be born in this range (Woosley and Heger, 2021). No black hole is expected to be inside this gap because of the pair-instability supernovae (PISNe), which disrupts the presupernova star and leaves no compact remnant (Farmer et al., 2019). The precise bounds of the PISNe mass gap are still uncertain (Fishbach and Holz, 2020) due to different nuclear reaction rates, evolution in detached binaries, rotation speed, and hyper-Eddington accretion for massive stars (Woosley and Heger, 2021). The lower bound is especially uncertain and varies in different papers (Marchant and Moriya, 2020; Woosley and Heger, 2021).

Intermediate-mass Black Hole (IMBH) refers to black holes with masses between [100, 10,000]$M_{\odot}$ (Greene, Strader, and Ho, 2020). These black holes are too

massive to form directly from stellar collapse or supernova, while not heavy enough to be supermassive black holes (SMBH) in the center of the galaxy. Therefore, the origin of these black holes remains unknown. In 2019, LIGO detected the first IMBH candidate GW190521 (R. Abbott et al., 2020b) with $m_1 = 95.3^{+28.7}_{-18.9} M_\odot$, $m_2 = 69.0^{+22.7}_{-23.1} M_\odot$, $m_f = 163.9^{+39.2}_{-23.5} M_\odot$ (L. S. Collaboration and V. Collaboration, 2021). The less massive IMBHs and BBHs in GW190521 all sit inside the PISNe mass gap, which should not be stable to maintain such mass (Woosley and Heger, 2021). Therefore, alternative theories of origins need to be established to explain the existence of black holes in the PISNe mass gap, including hierarchical merger and dynamical assembly (Safarzadeh, Farr, and Ramirez-Ruiz, 2020).

Lower Mass Gap

In addition to the PISNe mass gap, there is a lower-range mass gap within $[2.5, 5]M_\odot$ (R. Abbott et al., 2020c). The gap represents a dearth of observed compact objects, which comes from observational data of pulsar mass measurements and XRBs (Zevin et al., 2020). Inside this gap, the compact object population is unknown, which will be either the lightest black hole or the heaviest neutron star. Previous studies have explained this mass gap from the inefficiency of core-collapse supernovae and the internal structure of neutron stars (Sá et al., 2022). Although selection effects from observatories can induce some mass gaps, they cannot produce real observed mass gaps, which makes it a true characteristic of BH mass distribution (Özel et al., 2010).

However, LIGO detected a few GW events with compact objects in the lower mass gap such as GW190814 (R. Abbott et al., 2020c), which provides evidence against the existence of this mass gap (Sá et al., 2022). The common way to identify a compact object is to find its electromagnetic (EM) counterparts. NS-BH merger events are expected to have EM counterparts similar to BNS coalescence, while with imprints from the primary black hole. The disruption of NS and the formation of an accretion disk can cause gamma-ray bursts and kilonovae with ejections of neutron-rich matter. The color and luminosity of the EM signal reflect the black hole companion to help scientists identify a NS-BH merger event (Dichiara et al., 2021). In comparison, BBH mergers are expected to have no EM counterparts. However, seeking EM counterparts can be rare and coincidental (only one from GW170817 was found). Alternatively, we can use the NS equation of state (EoS) to compute the probability of the compact object as NS (R. Abbott et al., 2020c). The dimensionless deformation parameter κ is used to determine the compact object: κ

= 1 for Kerr BHs (Thorne, 1980) and κ = [2, 14] for NS (R. Abbott et al., 2020c). However, parameters in GW are characterized by posteriors, which can induce a large uncertainty on the κ value. The large error bar can make the κ value to span both the Kerr BH and the NS ranges, making it hard to judge the compact object populations.

Chapter 2

METHODOLOGY

In an earlier study (Hu et al., 2021), we introduced a new variable called the Merger Entropy Index ($\mathcal{I}_{\rm BBH}$), which characterizes the efficiency of entropy transfer during the binary black hole (BBH) merger:

$$\mathcal{I}_{\rm BBH} = \frac{\pi}{9}\frac{\Delta S_{BBH}}{S_1 + S_2}$$

where $\Delta S_{BBH} = S_f - (S_1 + S_2)$ measured the entropy change during the merger. As detailed in that study, this parameter is bounded by a **Theoretical Limit** imposed from general relativity such that

$$0 < \mathcal{I}_{\rm BBH} \leq 1$$

The parameter for a **Uniform Distribution of Circular** (**Uniform Prior**) BBH merger is bounded by

$$0 < \mathcal{I}_{\rm BBH} \leq 0.5$$

Both constraints relied on the assumption that the second law of thermodynamics (increase of entropy in BBH mergers) holds.

To apply $\mathcal{I}_{\rm BBH}$ to GW data, we follow the previously developed framework **BRAHMA** (**B**ina**R**y bl**A**ck **H**oles **M**erger entropy **A**nalysis) (Hu et al., 2021). This framework assumes all BBH mergers obey General Relativity and requires two datasets from the IMR analysis ($S_{1,2}$) and an independent measurement of the ringdown stage (S_f). The posterior distribution has a size of 1 × m for pre-merger and a size of 1 × n for post-merger, which enables the framework to construct a m × n matrix to fill in the $\mathcal{I}_{\rm BBH}$ values. Subsequently, the framework examines whether each data point satisfies the theoretical limit and the uniform prior. If the fraction of passed data exceeds the threshold ρ value, the framework keeps the row. Otherwise, the row will be discarded. Eventually, the framework outputs a filtered dataset (green wavelet in 2.1) of intrinsic parameters (Λ) and extrinsic parameters (Θ) with size of 1 × (m-i). The detailed schematic graph is available in (Hu et al., 2021). In principle, this

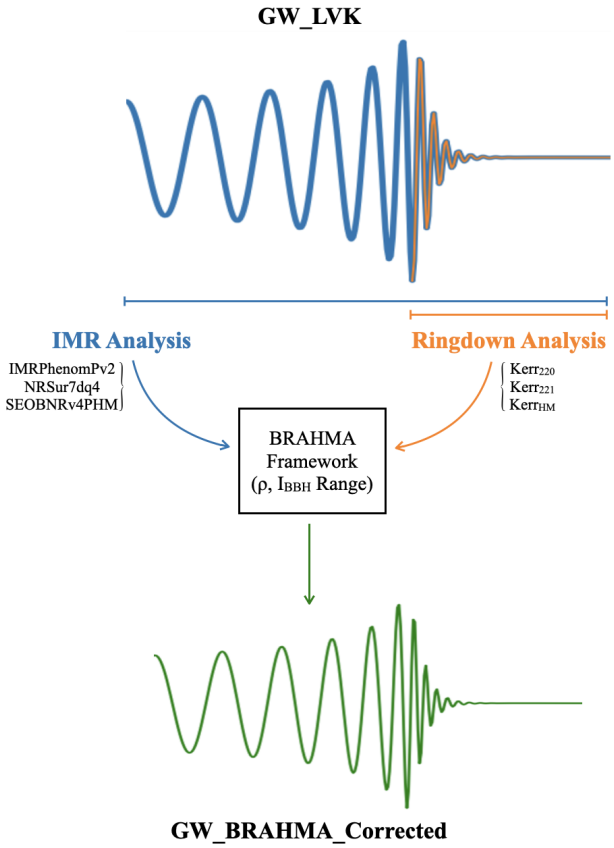

Figure 2.1: Schematic diagram of BRAHMA framework with different waveform and ringdown models. After inputting the original wavelet measured by LVK and an appropriate filter cut ρ, the framework generates a new GW wavelet confirmed by BRAHMA. The detailed schematic diagram of the BRAHMA framework can be found in (Hu et al., 2021).

approach is similar to the IMR consistency test (Abhirup Ghosh, Archisman Ghosh, et al., 2016), which computes the consistency between the wavelet and QNM and gains new insights from the difference.

IMR analysis characterizes the whole wavelet (blue wavelet in Fig. 2.1), while the independent ringdown measurement characterizes the ringdown stage only (orange portion in Fig. 2.1). As an IMR consistency test, we can input different waveform and ringdown models into the framework. The existing models and the schematic flow are shown in 2.1. We test 10 of the heaviest BBH merger events from LIGO-O3 (GWTC-2 & GWTC-3) with both the IMR analysis and the independent ringdown measures (L. S. Collaboration and V. Collaboration, 2021; L. S. Collaboration, V. Collaboration, and K. Collaboration, 2023), which allow us to seek new astrophysical insights. For each event, we use different waveforms and ringdown models (2.1).

The IMR ringdown model is inferred from the wavelet (IMR analysis), which will be completely consistent. Therefore, we do not include this ringdown model since it cannot obtain any new insight from the difference. In addition, the $\mathrm{Kerr}_{\mathrm{HM}}$ ringdown model cut off the parameters for most events, so we do not study them as well. The NRSur7dq4 waveform model is only available for certain events from GWTC-2. For events from GWTC-3, there is a Mixed waveform model, which integrates the Phenom and EOBNR families. Since this waveform model does not contain any new information apart from the combination of the other two models, we do not use this waveform in our analysis. Unless otherwise specified, the study uses the Kerr_{220} ringdown model and the SEOBNRv4PHM waveform (R. Abbott et al., 2020a). With different models, we also systematically investigate the consistency between phenomenological waveforms and ringdown models, as well as the effect of the filtering cut.

However, the original method of constructing matrices requires high computational capability, especially for events from GWTC-3. Such a large matrix occupies massive memories, resulting in broken kernels on locals. For most events, the original framework works only on HPC clusters. Therefore, we reduced the memory complexity and created an improved version of BRAHMA. Computing $\mathcal{I}_{\mathrm{BBH}}$ as an automatic variable, we could immediately evaluate and discard the specific value. Instead of using a matrix, we reversed the data structure as a list, which required less memory allocation. This improved version can now successfully run on locals for all GW events. Therefore, we plan to further develop the framework as a pipeline for future LIGO observing runs.

We have produced BRAHMA-corrected IMR posterior samples for public usages with the 10 heavier BBH merger events we tested (listed in Table 2.1). A new HDF5 (Hierarchical Data Format) file was created for each event. Within each .h5 file, there are two categories – LVK and Entropy. Accessing with the index key of **LVK**, the original posterior samples were directly measured by the gravitational wave detectors. If accessing with the index key of **Entropy**, the datasets will be BRAHMA corrected. In the Entropy category, the user can further choose whether they want to access the data imposed with the theoretical limit or uniform prior by using the keys **Theoretical** or **Uniform** respectively. Then, the user can get data with all the available phenomenological waveforms using the same name as listed in Table 2.1. Users can retrieve the desired data by accessing the index keys (names of the fields) in the GWTC. All the intrinsic parameters Λ and extrinsic parameters

Table 2.1: All events studied in this project with different waveform models and ringdown models.

Events	Waveform Models	Ringdown Models
GW190519	IMRPhenomPv2	IMR
	NRSur7dq4	Kerr_{220}
	SEOBNRv4PHM	Kerr_{221}
		Kerr_{HM}
GW190521	IMRPhenomPv3HM	IMR
	NRSur7dq4	Kerr_{220}
	SEOBNRv4PHM	Kerr_{221}
		Kerr_{HM}
GW190602	IMRPhenomPv2	IMR
	NRSur7dq4	Kerr_{220}
	SEOBNRv4PHM	Kerr_{221}
		Kerr_{HM}
GW190706	IMRPhenomPv2	IMR
	NRSur7dq4	Kerr_{220}
	SEOBNRv4PHM	Kerr_{221}
		Kerr_{HM}
GW190910	IMRPhenomPv2	IMR
	SEOBNRv4PHM	Kerr_{220}
		Kerr_{221}
		Kerr_{HM}
GW191109	IMRPhenomXPHM	Kerr_{220}
	SEOBNRv4PHM	Kerr_{221}
GW191222	IMRPhenomXPHM	Kerr_{220}
	SEOBNRv4PHM	Kerr_{221}
GW200129	IMRPhenomXPHM	Kerr_{220}
	SEOBNRv4PHM	Kerr_{221}
GW200224	IMRPhenomXPHM	Kerr_{220}
	SEOBNRv4PHM	Kerr_{221}
GW200311	IMRPhenomXPHM	Kerr_{220}
	SEOBNRv4PHM	Kerr_{221}

Θ in the Entropy category need to be accessed with the keys **parameter_filtered**. The default filtering cut ρ is 75, which is shown to be optimal in later sections, and the default ringdown model is Kerr_{220}. We have put the datasets on Zenodo.

For example, if the user wants to access the BRAHMA corrected inclination angle with the theoretical limit and SEOBNRv4PHM waveform:

```
results = h5py.File('GW191222_Entropy.h5', 'r')
iota_BRAHMA = results['Entropy']['Theoretical']
                    ['SEOBNRv4PHM']['iota_filtered']
```

For other GW events from GWTC-2 & GWTC-3 without an independent ringdown analysis, the ringdown phase can be interpreted by perturbation theory on the Kerr spacetime background (Flanagan and Hughes, 1998). Both the QNM and IMR post-merger measurements show agreement with Hawking area theorem (Correia and Capano, 2023). Therefore, we can obtain the intrinsic parameters including mass and spin of the remnant black holes solely with the IMR analysis, enabling us to compute the $\mathcal{I}_{\mathrm{BBH}}$ value for all GW events. Then, we can compute the $\mathcal{I}_{\mathrm{BBH}}$ distributions for all GW events and obtain a combined posterior for $\mathcal{I}_{\mathrm{BBH}}$.

Gravitational wave detectors can cause selection effects. GW sources are more likely to come from certain sky localization or certain times during the duty cycle. The sensitivity regions for the two LIGO detectors are above North America and the Indian Ocean. As the Earth rotates, the region will swipe the entire sky localization. Meanwhile, the detectors have the preference to collect data at night (H.-Y. Chen et al., 2017). These factors can all cause bias when constructing the distribution of $\mathcal{I}_{\mathrm{BBH}}$ for compact object populations. To correct for selection effects, we have to perform population analyses. Therefore, we adopt the Power Law + Peak model for gravitational wave populations (Talbot and Thrane, 2018), which demonstrates the highest Bayes factor in characterizing the GWTC-3 dataset (L. S. Collaboration, V. Collaboration, and K. Collaboration, 2023). The model assumes that spin and mass are independent and uncorrelated. Therefore, the hyperposterior gives different distributions to describe m_1, q (mass & mass ratio), χ_1, χ_2 (spin magnitude), and z (redshift). By implementing the reverse CDF (cumulative distribution function) sampling and rejection sampling, we draw 10,000 individual merger samples from the distributions derived from gravitational wave observations. Such a large number of samples ensures the accuracy of population estimations and recovers the true astrophysical population. These mergers are BBH mergers with masses between

[2.5, 100]$M_\odot$ in the source frame and spin between [0, 1]. The population modeling gives us measurements of the pre-merger parameters.

Numerical relativity solves Einstein's equations of general relativity, which characterize the gravitational wavelet with high accuracy. Therefore, we utilize the **NRSur7dq4Remnant** fit from the SurfinBH (**Su**rrogate **fin**al **B**lack **H**ole) package derived from numerical relativity (Varma, Gerosa, et al., 2019). This package estimates the properties of the remnant black holes. Inferred from the pre-merger parameters, the package approximates the final mass, spin, and recoil kick velocity.

With the pre-merger entropy calculated from Power Law + Peak and the post-merger entropy calculated from the SurfinBH package, we can compute $\mathcal{I}_{\mathrm{BBH}}$ distributions for BBH mergers. $\mathcal{I}_{\mathrm{BBH}}$ generally does not work for BNS coalescence or NS-BH merger due to a lack of measurements for post-merger, so we exclude confirmed events apart from BBH mergers when computing the overall posterior.

Chapter 3

"BRAHMA WITH RINGDOWN" – SEEKING NEW ASTROPHYSICAL INSIGHTS WITH $\mathcal{I}_{\rm BBH}$

3.1 Impact on PISNe Mass Gap

The PISNe mass gap has an uncertain range, especially for the lower bound (Marchant and Moriya, 2020; Woosley and Heger, 2021). Therefore, we adopt two intervals in our study: [60, 130]$M_\odot$ and [40, 130]$M_\odot$. Although black holes theoretically should not have mass inside this gap, LIGO still detects several BBH merger events inside this gap (shown in Fig. 3.1) (O'Brien et al., 2021). We apply our BRAHMA framework to these events to test whether thermodynamics supports the existence of black holes inside the PISNe mass gap. From the left plot, we can observe that the m_1 posterior with the theoretical limit derived from general relativity imposed (green region) generally decreases compared to the original posterior (red region). However, the decrease is minor and most data still remains inside the PISNe gap. The right figure shows a quantitative version of the m_1 posterior distribution. The probability indicates the fraction of data inside the PISNe mass gaps. This plot also adds the posterior with the uniform prior imposed (red bars), which is similar

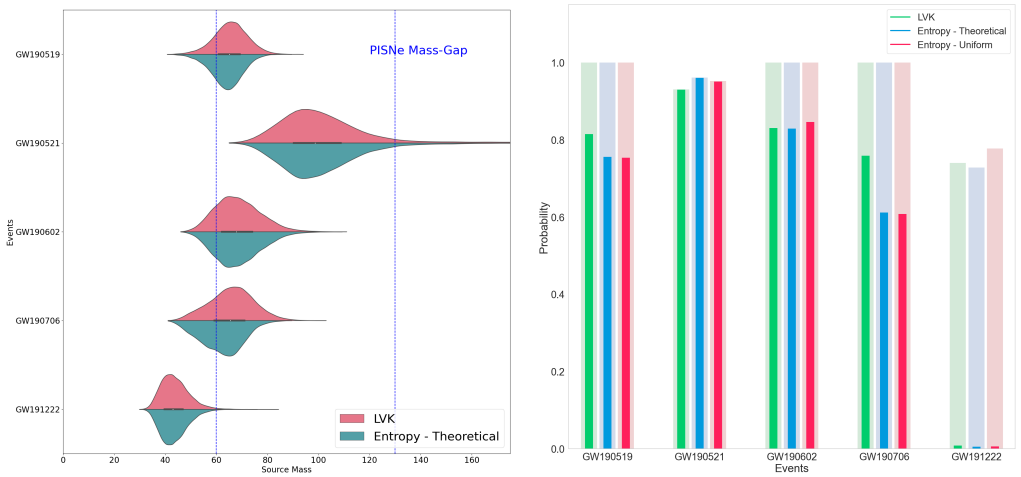

Figure 3.1: The left graph shows the $m_{1,src}$ posterior distribution with selected heaviest GW events. The two blue dotted lines denoted the PISNe mass gap of [60, 130] $M_\odot$. The right graph shows the probability P($60M_\odot \leq$ m $\leq 130M_\odot$) (bright bars) and P(40 $M_\odot \leq$ m $\leq 130M_\odot$) (fainter bars) for posteriors measured by LVK, posteriors with the theoretical limit, and posteriors with the uniform prior

to the posterior with the theoretical limit. Two intervals for PISNe mass gaps are used: [60, 130]$M_\odot$ (brighter bars) and [40, 130]$M_\odot$ (fainter bars). Quantitatively, the probability only changes slightly after imposing thermodynamical constraints, except GW190706 – P($60M_\odot \leq$ m $\leq 130M_\odot$) decreases approximately from 75% to 60% when applying the constraints. However, more than half of the data still remains in the PISNe mass gap. If we look for P($40M_\odot \leq$ m $\leq 130M_\odot$), GW190706 does not show significant change after adding constraints. Therefore, this event will not be an outlier to our conclusion. We independently use entropy to prove the existence of black holes inside the PISNe mass gap. This result demonstrates that thermodynamics supports the feasibility of black holes inside the PISNe gap, which provides us with insights into the origins of these heavier stellar mass black holes. If the PISNe model is correct, we will need to find alternative theories to explain the formation channels.

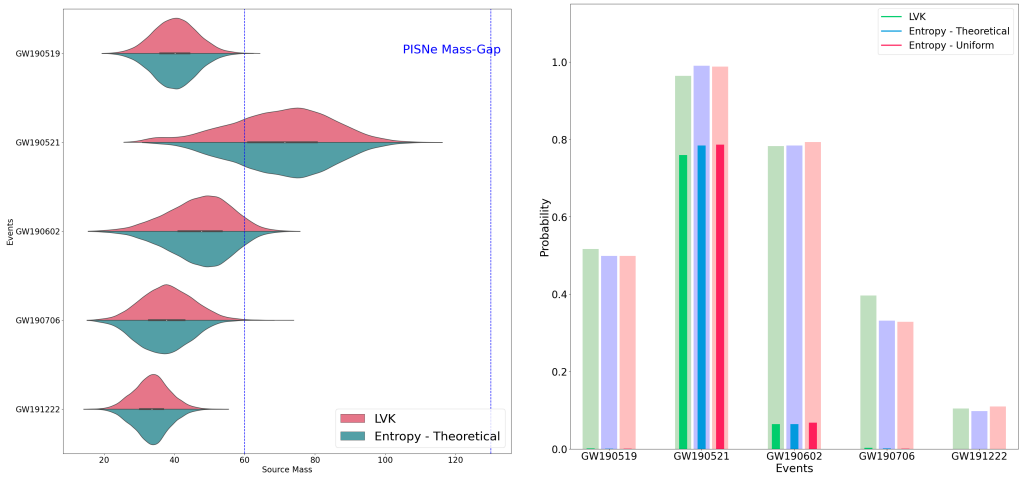

Figure 3.2: Similar to Fig. 3.1, the left plot shows the $m_{2,src}$ posterior distribution. The right plot shows the probability P($60M_\odot \leq$ m $\leq 130M_\odot$)(brighter bars) and P($40M_\odot \leq$ m $\leq 130M_\odot$) (fainter bars)

Similarly, we compute the m_2 posterior distribution in the source frame (Fig. 3.2). Secondary black holes are always lighter than the primary black holes, so most data is outside the PISNe mass gap apart from GW190521 (R. Abbott et al., 2020b). Looking at the right plot, we can see thermodynamical constraints do not affect the fraction of data inside the PISNe mass gap regardless of which intervals are used. Previously, the BRAHMA framework sought new astrophysical insights regarding this event. The bimodality behavior is no longer present in the q-$\chi_{\rm eff}$ parameter space after imposing thermodynamical constraints, which also gives insights into the lower bounds and P(z $\leq$ AGN) (Hu et al., 2021). Such bimodality behavior

occurs in the m_2 posterior distribution plot in Fig. 3.2, with a small peak of $35M_\odot$ and a large peak of $66M_\odot$. The BRAHMA framework removed the small peak after adding the theoretical limit, suggesting that this high probability measure of $m_2 = 35M_\odot$ does not obey general relativity. This phenomenon is responsible for the new astrophysical insights found in the q-$\chi_{\rm eff}$ parameter space shown in the paper (Hu et al., 2021). This small peak is also outside both intervals of $[60, 130]M_\odot$ and $[40, 130]M_\odot$, so removing the peak slightly increases the probability of m_2 inside the PISNe mass gap, which gives another robust indication that black holes can exist in the PISNe mass gap according to thermodynamics. The small peak of $35M_\odot$ is consistent with the Power Law + Peak model (Talbot and Thrane, 2018), which suggests such a peak more likely comes from artifacts and the selection effects of LIGO detectors.

3.2 New Astrophysical Insights with GW191109

$\mathcal{I}_{\rm BBH}$ is particularly good at differentiating between different formation channels. Previously, we found some new astrophysical insights with GW190521, the heaviest confirmed BBH merger (Hu et al., 2021). After applying the BRAHMA framework associated and imposing thermodynamical constraints on the other 9 heaviest events, GW191109 also showed some new astrophysical insights (Fig. 3.3).

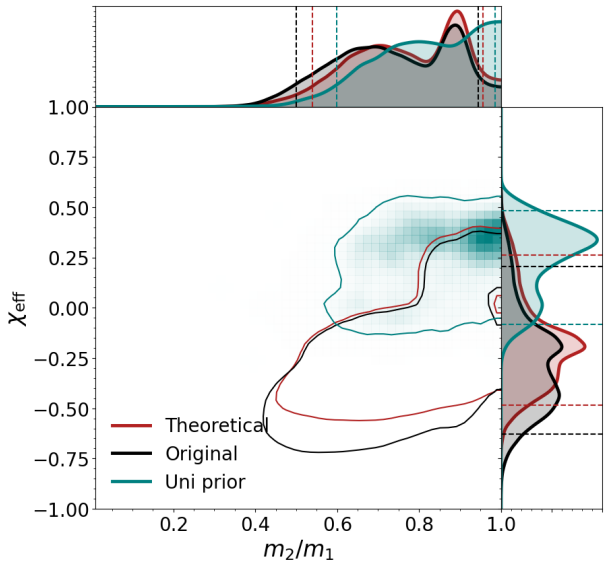

Figure 3.3: KDE plot of GW191109 with IMRPhenomXPHM waveform and Kerr$_{220}$ ringdown model in q-$\chi_{\rm eff}$ parameter space

The effective spin of the BBH merger measures the alignment between the spins and the angular momentum (B. P. Abbott et al., 2016b), which is characterized by

the individual spin and mass of two pre-merger black holes:

$$\chi_{\rm eff} = \frac{(m_1\chi_1 + m_2\chi_2)\cdot \hat{L}_N}{m_1 + m_2} = \frac{(\chi_1 + q\chi_2)\cdot \hat{L}_N}{1+q}$$

where $\hat{L}_N$ is the unit vector along the orbital angular momentum. The effective spin is constrained in the range [-1, 1]. However, most binaries from field formations detected by LVK have positive $\chi_{\rm eff}$. GW191109 shows an unusual negative $\chi_{\rm eff}$ of -0.29 (Zhang et al., 2023). The lower bound even reaches -0.7 (black contour shown in Fig. 3.3). When applying the thermodynamical constraints, $\chi_{\rm eff}$ increases, especially for the uniform prior (green contour). The theoretical limit (red contour) derived from general relativity also slightly increases $\chi_{\rm eff}$ for the lower bound. Therefore, if such negative $\chi_{\rm eff}$ is measured and derived correctly, GW191109 may not satisfy the quasi-circular hypothesis of LIGO, and we cannot rule out the possibility that the pre-merger black holes obtain an eccentric non-circular orbit (Romero-Shaw, Lasky, and Thrane, 2022). In this case, the primary black hole with $65M_\odot$, which is in the PISNe mass gap, tends to form by dynamical assembly. The negative $\chi_{\rm eff}$ value and the heavy source mass successfully fit into the symmetric expected distribution of dynamical assembly (Safarzadeh, Farr, and Ramirez-Ruiz, 2020).

However, GW191109 suffers from glitches and data quality issues, which may cause false measurements of the spin (R. Abbott et al., 2021c; Wang et al., 2022), so we cannot rule out the possibility of imposing the event to fit into the quasi-circular hypotheses. In this case, the median $\chi_{\rm eff}$ increases to around 0.2, which becomes consistent with the BBH populations. Then, the heavy black holes tend to form as a field binary in an isolated system. The primary black hole inside the PISNe mass gap may be a second-generation black hole that merges again within Hubble time t_H (Safarzadeh, Farr, and Ramirez-Ruiz, 2020). Such a formation channel largely associates with the established hierarchical merger hypothesis (Antonelli et al., 2023).

Regardless of formation channels, the posterior of the theoretical limit (red contour) in the q-$\chi_{\rm eff}$ parameter space relatively agrees with the original posterior measured by LVK, showing GW191109 still obeys relativity despite the unusual effective spin. This qualitative approach can be developed further by computing the degree of consistency between the original posterior and the posterior imposed by the theoretical limit, which can give additional selection criteria for GR testing in LIGO

(appeared in R. Abbott et al., 2021c). This plot also gives us perspectives on using $\mathcal{I}_{\rm BBH}$ and the BRAHMA framework to test general relativity for BBH mergers from thermodynamic aspects.

3.3 Impact of Filtering Cut

The dataset with filtered parameters Λ and Θ should contain at least 10% of the original data measured by LVK to be valid and reliable. Based on this threshold, we test and determine that the optimal filtering cut ρ should be around 75%. If only considering the theoretical limit derived from general relativity, ρ can reach 80%. The framework combines IMR analysis and ringdown analysis. The filtering cut is an indication of the consistency between the phenomenological waveform and the ringdown model. Using $\mathcal{I}_{\rm BBH}$ as an indicator, the consistency between the phenomenological waveform and the ringdown model is thus 75%. The framework relies on the assumption that the ringdown measurement (QNMs) gives a more robust model of the post-merger condition, which gives astrophysical implications, including eccentric orbits and dynamic captures. We need to seek the inconsistency between the pre-merger measurement and the post-merger measurement to extract these astrophysical insights. Therefore, choosing an appropriate filtering cut ρ becomes especially important.

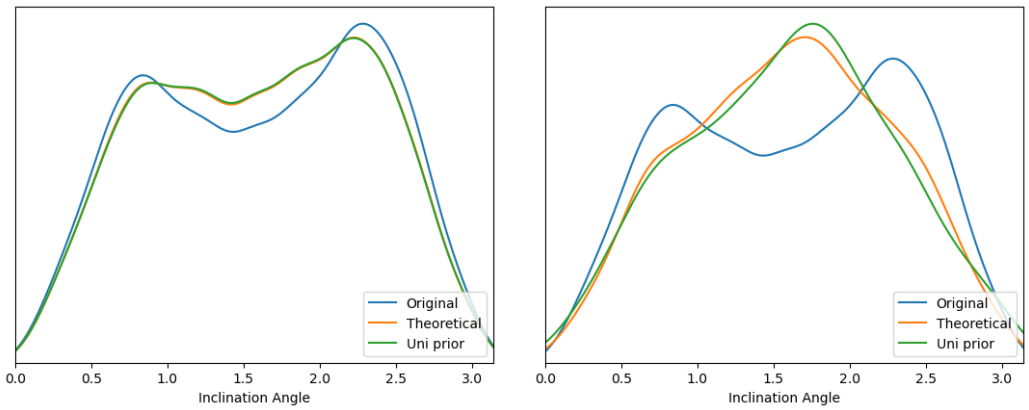

Figure 3.4: 1-D KDE histogram plots of the inclination angle of GW190519. The left plot has a filtering cut ρ = 75, and the right plot has a filtering cut ρ = 95.

An inappropriate ρ value can result in faulty astrophysical insights. For GW190519 with the NRSur7dq4 waveform and Kerr$_{221}$ ringdown model, the bimodality behavior exists in the inclination angle parameter space. With high filtering cuts, two peaks merge to one broad peak after imposing thermodynamical constraints (the right plot of Fig. 3.4). The higher the filtering cut, the sharper the peak is. However,

this removal of bimodality does not appear for the lower filtering cut (the left plot of Fig. 3.4). Such astrophysical insights depend on filtering cuts, which are not robust and should not be considered as an astrophysical insight provided by entropy. In contrast, the astrophysical insight (bimodality behavior removal) of GW190521 exists with every filtering cut ρ. Even with a filtering cut of 60%, the small peak at around $35M_{\odot}$ disappears after applying the thermodynamical constraints. In fact, GW190521 is a special event: the filtering cut ρ makes trivial effects on the parameters. From the detection perspective, the BBH merger of GW190521 is observed closely, resulting in higher consistency between the posterior measured by LVK and the posterior with thermodynamical constraints. Higher modes are available in GW190521, which gains more agreement (R. Abbott et al., 2020b). This consistency is remarkable for the theoretical limit, over 95% of GW data satisfies the constraints with any filtering cut between [60%, 99%], showing the BBH merger strongly obeys general relativity. Over 25% of data remains after imposing a uniform prior for every waveform and ringdown model, so the merger very likely follows a circular orbit in the inspiral stage, which is compatible with the quasi-circular hypothesis.

Different filtering cuts result in different extents of consistency, which leads to different conclusions. At the standard filtering cut of 75%, GW190706 shows higher consistency with the Kerr_{HM} ringdown model than the Kerr_{220} ringdown model, which is opposite to the conclusion drawn from the Bayes factor in the TGR paper (R. Abbott et al., 2021c). However, when switching to a higher filtering cut of around 90%, which is the same as LIGO's confidence interval on model parameters, Kerr_{220} gives higher agreement than the Kerr_{HM} ringdown model as expected. Careful selections of the filtering cut ρ are required to test different models.

3.4 Impact of QNM for Ringdown

If using the optimal filtering cut of 75%, which enables every dataset filtered by BRAHMA to become valid, the Kerr_{221} ringdown model has the highest consistency with the original GW posterior across all BBH merger events we studied. The IMR ringdown model is consistent with the phenomenological waveform, which does not give meaningful results in the BRAHMA framework and the IMR consistency test. The Kerr_{HM} ringdown model completely cuts off the parameter for several events we studied at $\rho = 75\%$, so these two ringdown models are not considered the optimal model for our analysis. We compute a statistical test on the remaining two ringdown models Kerr_{220} & Kerr_{221} (Table 3.1). The logarithm of the agreement

Table 3.1: Statistical test between Kerr_{220} and Kerr_{221} ringdown models for all waveform models across BBH merger events. The fraction shows the percentage of consistency between the original posterior measured by LVK and the posterior with the theoretical limit, and we compute the logarithm of the ratio.

Event	Waveform	Kerr_{220}	Kerr_{221}	$\log_{10}(\frac{\text{Kerr}_{220}}{\text{Kerr}_{221}})$
GW190519	IMRPhenomPv2	0.21	0.51	-0.4
	NRSur7dq4	0.29	0.62	-0.3
	SEOBNRv4PHM	0.18	0.45	-0.4
GW190521	IMRPhenomPv3HM	0.99	0.99	0
	NRSur7dq4	1	1	0
	SEOBNRv4PHM	0.96	0.96	0
GW190602	IMRPhenomPv2	0.83	0.91	0
	NRSur7dq4	0.87	0.94	0
	SEOBNRv4PHM	0.85	0.93	0
GW190706	IMRPhenomPv2	0.03	0.65	-1.3
	NRSur7dq4	0.06	0.72	-1.1
	SEOBNRv4PHM	0.03	0.59	-1.3
GW190911	IMRPhenomPv2	0.99	1	0
	SEOBNRv4PHM	1	1	0
GW191222	IMRPhenomXPHM	0.25	0.85	-0.5
	SEOBNRv4PHM	0.21	0.82	-0.6
GW200129	IMRPhenomXPHM	0.87	1	-0.1
	SEOBNRv4PHM	0.79	1	-0.1
GW200224	IMRPhenomXPHM	0.81	1	-0.1
	SEOBNRv4PHM	0.69	1	-0.2
GW200311	IMRPhenomXPHM	0.83	0.98	-0.1
	SEOBNRv4PHM	0.95	0.97	0

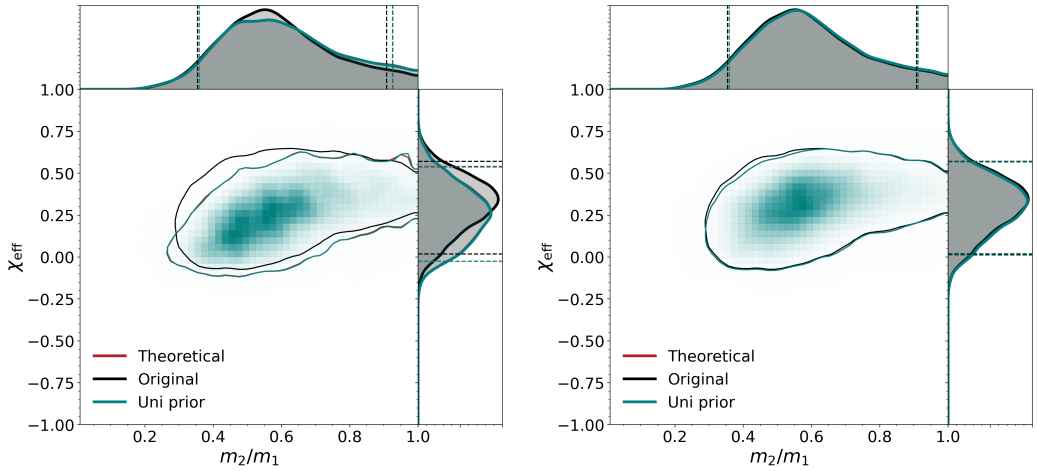

Figure 3.5: Effect of ringdown models shown on GW190706, displaying the KDE plot in the q-$\chi_{\rm eff}$ parameter space with Kerr_{220} (left plot) and Kerr_{221} (right plot) ringdown models

ratio is calculated. A positive value indicated that Kerr_{220} agreed more than Kerr_{221}, and a negative value showed that Kerr_{221} had higher agreement. We can clearly see that Kerr_{221} agrees more for all events. The effect of different ringdown models is visualized in Fig. 3.5 for GW190706, which differentiates the ringdown models most according to the statistics shown in Table 3.1. In the q-$\chi_{\rm eff}$ parameter space, the Kerr_{221} ringdown model (right plot) shows significantly higher consistency with SEOBNRv4PHM waveform than the Kerr_{220} ringdown model (left plot).

The high consistency of Kerr_{221} is different from our expectation that Kerr_{220} should be the dominant ringdown model in LIGO (Abhirup Ghosh, Brito, and Buonanno, 2021). Kerr_{221} incorporates the first overtone ($\pm m$) in addition to the fundamental modes (R. Abbott et al., 2021c). Recent NR simulations suggest that the ringdown stage can happen slightly earlier than we would expect. The oscillation of spacetime (ringdown) can start early in the merger stage, which can only be characterized when $n \geq 1$ (Forteza and Mourier, 2021). Our result of highest consistency with Kerr_{221} supports the early ringdown start time and overlap between merger and ringdown stages from NR simulations. In addition, the BRAHMA framework shows low consistency between phenomenological waveform and the $\text{Kerr}_{\rm HM}$ ringdown model, especially when the mass ratio approaches 1, showing the absence of higher-order modes in GW events.

3.5 Impact of IMR Waveform Models

Waveform models from the IMR analysis do not have a large effect on the posterior as the ringdown models. If the parameters for a BBH merger are completely cut off with the IMRPhenomPv2 waveform model, generally it will cut off parameters for NRSur7dq4 and SEOBNRv4PHM waveforms as well. However, different waveform models will have different percentages of consistency with the original event. NRSur7dq4 agrees the most when it is available from the LVK datasets. For GW190521, the difference between waveform models was marginal (less than 1%), yet NRSur7dq4 remains the most agreed model. For the 6 events from GWTC-3, NRSur7dq4 does not exist due to the restricted number of inspiral orbits (L. S. Collaboration, V. Collaboration, and K. Collaboration, 2023). In this case, IMRPhenomXPHM either agrees more than SEOBNRv4PHM, or the difference between these two models was less than 1%. The only exception was GW200311 with the Kerr_{220} ringdown model, in which 83% of the data remains for the IMRPhenomXPHM waveform model and 98% of the data remained for the SEOBNRv4PHM waveform model. There is no significant difference between IMRPhenomXPHM and SEOBNRv4PHM waveforms for us to draw a valid conclusion.

NRSur7dq4 is generated from numerical relativity simulations, which does not depend on the IMR phenomenological fit or EOB formalism (Islam et al., 2023). From our BRAHMA framework, waveforms from numerical relativity simulations display the highest consistency as expected. Since the waveform is fit as a solution to Einstein's General Relativity, most data should satisfy our established theoretical limit, which is derived from general relativity. For GW190521, the difference between waveforms can be marginal due to higher-frequency subdominant modes (Capano et al., 2023). The characteristic of NRSur7dq4 may account for higher consistency, which indicates the importance of numerical relativity in gravitational wave study. How well we can solve Einstein's general relativity equation from the numerical relativity simulation determines the sensitivity and range of the gravitational wave detectors, which is fundamental. However, solving such equations can be computationally expensive, so not all events have such a fitted waveform. The phenomenological fit will have a higher consistency with the original event than the effective one-body formalism from our study. However, since our sample size with the NRSur7dq4 waveform is small (only 4 events), we cannot give a very solid conclusion until more numerical relativity simulation data are available for future detection.

Chapter 4

"BRAHMA WITHOUT RINGDOWN" – DIFFERENTIATING COMPACT BINARY POPULATIONS WITH $\mathcal{I}_{\rm BBH}$

4.1 Astrophysical Distribution of $\mathcal{I}_{\rm BBH}$

For events without an independent ringdown measurement due to low SNR, we obtain the post-merger parameters from the phenomenological waveform as introduced in Chapter 2. We exclude all confirmed BNS coalescence (B. P. Abbott et al., 2019) and NS-BH merger events (R. Abbott et al., 2021a). For other observations, we model the $\mathcal{I}_{\rm BBH}$ posterior (grey curves in Fig. 4.1). Because $\mathcal{I}_{\rm BBH}$ generally only works for BBH merger events, other types of compact object coalescence can make outlier distributions. NS-BH merger events like GW191219 and GW200105 (L. S. Collaboration, V. Collaboration, and K. Collaboration, 2023) will display a sharp spike at $\mathcal{I}_{\rm BBH} \approx 0.1$. However, there are some events where the secondary object remains unknown, which can be potential NS-BH merger events or other compact object coalescence (In Section 4.3, we will elaborate more details about these events). These events will have different $\mathcal{I}_{\rm BBH}$ distributions, so there are several posteriors in the lower $\mathcal{I}_{\rm BBH}$ value range. These posteriors also account for the small fluctuations in the observed population of LIGO. For larger values of $\mathcal{I}_{\rm BBH}$, the notable distribution on the rightmost of Fig. 4.1 comes from GW191109, which has a highly negative $\chi_{\rm eff} \approx$ -0.29 (Zhang et al., 2023). In Section 3.3, when we use an independent ringdown measurement to characterize the post-merger stages, the $\mathcal{I}_{\rm BBH}$ of GW191109 exceeds 0.5, showing incompatibility with the quasi-circular hypothesis. However, when using the IMR analysis only, the $\mathcal{I}_{\rm BBH}$ values should always be ≤ 0.5 because the waveform is imposed to comply with the uniform prior. There will be no inconsistency between the inspiral and ringdown stages without the ringdown model, yet the $\mathcal{I}_{\rm BBH}$ posterior is still large compared with other events due to the highly negative $\chi_{\rm eff}$.

To correct selection effects, we did a population analysis with reverse CDF sampling and numerical relativity fits, as detailed in Chapter 2. The black line in Fig. 4.1 shows the astrophysical prior with selection effects corrected. We can notice that the observed population of LIGO spans a larger range of $\mathcal{I}_{\rm BBH}$ values than the true population. The lower range comes from compact object coalescence with

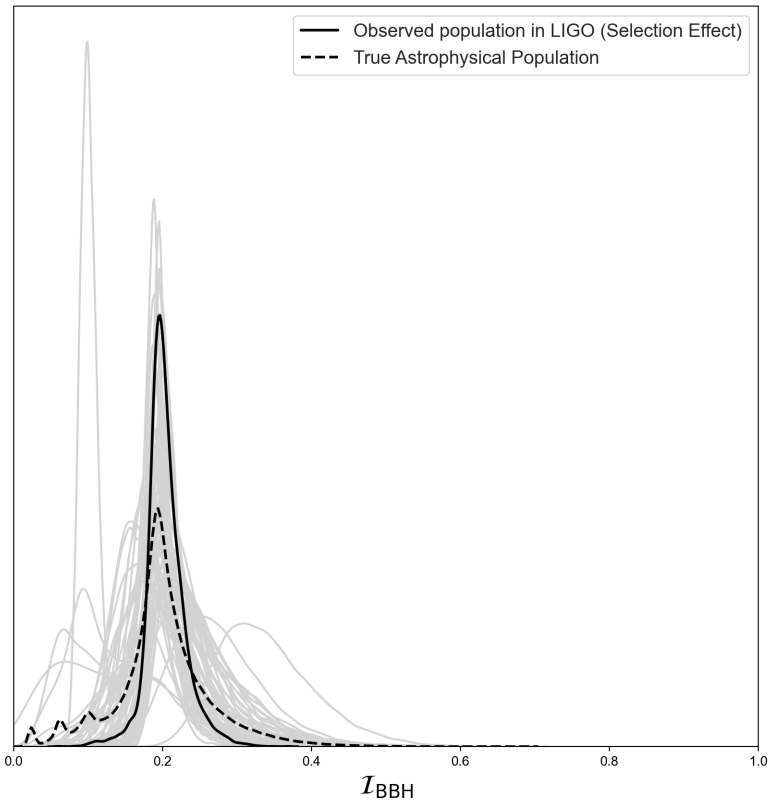

Figure 4.1: Astrophysical distribution of $\mathcal{I}_{\rm BBH}$ values. Grey lines show the individual $\mathcal{I}_{\rm BBH}$ posteriors of GW events detected by LVK. The dotted black line shows their combined posterior without any bias correction, while the solid black line shows the true astrophysical population with selection effects corrected by sampling 10,000 points from the GWTC-3 population.

an unknown secondary object in the lower mass gap, and the higher range comes from heavier stellar-mass black holes or IMBHs. The sample size for the combined astrophysical prior is 84, which is the total number of BBH mergers detected until O3. To correct the selection effects, we sample 10,000 data points from GWTC-3 populations. The astrophysical prior with selection effects corrected resembles a Gaussian distribution due to the central limit theorem, with a median at $\mathcal{I}_{\rm BBH} \approx 0.2$, which overlaps with many GW posteriors shown in grey. With more GW events detected by LVK in the future, we will expect the dotted line to become a Gaussian distribution like the solid line, while extending a larger range of $\mathcal{I}_{\rm BBH}$ between [0, 0.7].

We also compute the cumulative distribution of both the observed and true astrophysical populations of LIGO. The prior with selection effect corrected is the same as Fig. 4.2 in our earlier study (Hu et al., 2021). The observed population resembles

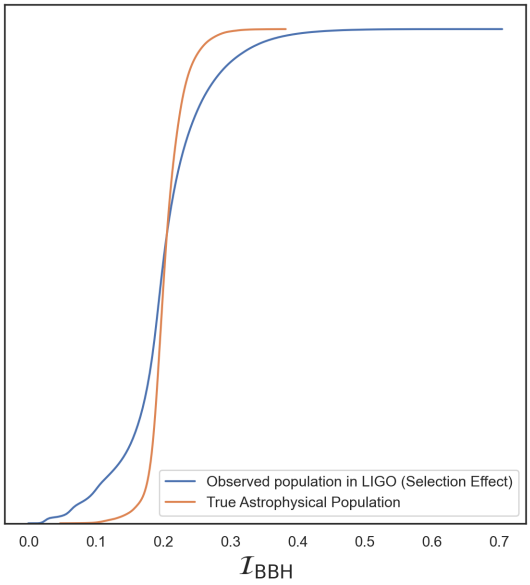

Figure 4.2: CDF of $\mathcal{I}_{\mathrm{BBH}}$ for observed and true populations of LIGO BBH

the uniform prior presented in our previous study. Uniform prior characterizes the uniform distribution of circular BBH mergers. The searching and parameter estimation algorithms of LVK could only model waveforms as circular binaries (Setyawati and Ohme, 2021). IMR analysis has data based on the quasi-circular hypothesis, so computing $\mathcal{I}_{\mathrm{BBH}}$ values from IMR analysis only will always satisfy the uniform prior. As in Fig. 4.1, the combined astrophysical prior spans a larger range of $\mathcal{I}_{\mathrm{BBH}}$ [0, 0.5]. Therefore, the combined astrophysical prior will have a similar distribution as the uniform prior. The true astrophysical population with selection effects corrected (orange distribution in Fig. 4.2) has a sharp increase at $\mathcal{I}_{\mathrm{BBH}} \approx 0.2$: a small change of $\mathcal{I}_{\mathrm{BBH}}$ can result in a large difference in the CDF. Such an increase suggests that $\mathcal{I}_{\mathrm{BBH}}$ has a strong capacity for differentiating. $\mathcal{I}_{\mathrm{BBH}}$ values can largely vary with the mass, especially between stellar-mass black holes and supermassive black holes, which corresponds to different origins and formation channels (Hu et al., 2021). Based on this property, we will explore the potential use of the Merger Entropy Index to differentiate different compact binary populations.

From such $\mathcal{I}_{\mathrm{BBH}}$ distributions, we can introduce an astrophysical prior rather than the theoretical limit and uniform prior we implemented. This astrophysical prior is derived from the constraints on mass and spin for the observed BBH population in GWTC-3 (L. S. Collaboration, V. Collaboration, and K. Collaboration, 2023). The $\mathcal{I}_{\mathrm{BBH}}$ values for the population centers at 0.2 (shown in Fig. 4.1). With a 99%

confidence interval:

$$0 \leq \mathcal{I}_{\mathrm{BBH}} \leq 0.3$$

As suggested, the astrophysical prior can vary between supermassive and stellar mass BBH populations (Hu et al., 2021), which can be an important indication of population classification and formation channels. Therefore, we will use $\mathcal{I}_{\mathrm{BBH}}$ to differentiate between compact populations in this study.

4.2 Differentiate IMBH/Heavy-Mass Black Holes from Stellar-Mass Black Holes

We filtered only the confirmed BBH merger events from both GWTC-2 & GWTC-3 (L. S. Collaboration and V. Collaboration, 2021; L. S. Collaboration, V. Collaboration, and K. Collaboration, 2023). We classify them into two categories based on their mass in the source frame – heavy-mass & stellar-mass black holes. Shown in Fig. 4.3, we classify with both the primary black hole $m_{1,\mathrm{src}}$ and the secondary black hole $m_{2,\mathrm{src}}$.

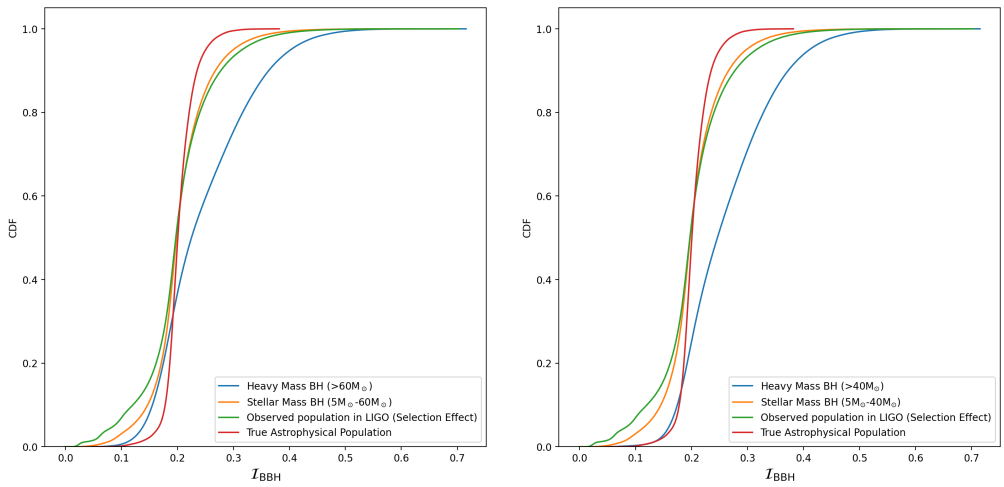

Figure 4.3: Cumulative distribution functions of $\mathcal{I}_{\mathrm{BBH}}$ for confirmed BBHs with the astrophysical priors as reference. The left plot classifies BBHs based on the primary mass $m_{1,\mathrm{src}}$ with $60M_\odot$ as a threshold, and the right plot classifies BBHs based on the secondary mass $m_{2,\mathrm{src}}$ with $40M_\odot$ as a threshold.

Because lower-mass black holes (5-40$M_\odot$) constitute the majority of the observed populations from LIGO, the $\mathcal{I}_{\mathrm{BBH}}$ CDF for the observed population in LIGO with selection effects is very close (nearly overlaps) to the $\mathcal{I}_{\mathrm{BBH}}$ CDF of stellar-mass black holes (orange and green lines in Fig. 4.3). We conduct Kolmogorov–Smirnov (KS)

Table 4.1: $\mathcal{D}$ values from KS-Test for the primary black holes.

CDF	Observed $\mathcal{I}_{\rm BBH}$	True $\mathcal{I}_{\rm BBH}$	Stellar-Mass BH	Heavy BH
Observed $\mathcal{I}_{\rm BBH}$	/	0.20	0.05	0.24
True $\mathcal{I}_{\rm BBH}$	0.20	/	0.16	0.36
Stellar-Mass BH	0.05	0.16	/	0.26
Heavy BH	0.24	0.36	0.26	/

Table 4.2: $\mathcal{D}$ values from KS-Test for the secondary black holes.

CDF	Observed $\mathcal{I}_{\rm BBH}$	True $\mathcal{I}_{\rm BBH}$	Stellar-Mass BH	Heavy BH
Observed $\mathcal{I}_{\rm BBH}$	/	0.20	0.05	0.33
True $\mathcal{I}_{\rm BBH}$	0.20	/	0.17	0.45
Stellar-Mass BH	0.05	0.17	/	0.35
Heavy BH	0.33	0.45	0.35	/

tests on the CDFs shown in Fig. 4.3, and the results are shown in Table 4.1 & Table 4.2. $\mathcal{D}$ is a measure of the maximum distance between CDFs. When comparing two CDFs (datasets), the $\mathcal{D}$ value is calculated as:

$$\mathcal{D}_{n,m} = \sup_x |F_{1,n}(x) - F_{2,m}|$$

where $F_{1,n}(x)$ is the CDF for the first dataset n and $F_{2,m}(x)$ is the CDF for the second dataset m. "$\sup_x$" helps to obtain the maxima from the set of the distance. $\mathcal{D}$ for stellar-mass black holes & the observed population in LIGO is only 0.05, which suggests a very trivial difference. In contrast, the heavy-mass black holes deviate from both astrophysical priors and the $\mathcal{I}_{\rm BBH}$ CDF of stellar-mass black holes. The difference between the $\mathcal{I}_{\rm BBH}$ CDF of heavier-mass black holes and the true astrophysical population shows a large $\mathcal{D}$ value of 0.45 when classifying based on the secondary black hole (4.2). Such a difference is significant: for the right plot in Fig. 4.3 that classifies with $m2$_src, nearly 100% of the data that forms the astrophysical prior with selection effects corrected has $\mathcal{I}_{\rm BBH}$ smaller than 0.25. The posterior of stellar-mass black holes also shows that over 90% $\mathcal{I}_{\rm BBH}$ data is smaller than 0.25. In comparison, heavy-mass black holes have relatively larger $\mathcal{I}_{\rm BBH}$, with only half of the $\mathcal{I}_{\rm BBH}$ data smaller than 0.25. The increase of the probability is also quite gentle for heavy-mass black holes. This differentiation supports that heavier-mass black holes can correspond to some different origins and formation channels. Although we use different threshold masses to classify heavy mass for primary ($60M_\odot$) and secondary ($40M_\odot$) black holes, they should have a similar

classification. The lower bound of the PISNe mass gap is uncertain between [40, 65]$M_\odot$(Marchant and Moriya, 2020; Woosley and Heger, 2021). No matter at $40M_\odot$ or $60M_\odot$, the black holes should be unstable to be formed directly by stellar collapse. Therefore, both our thresholds should lead to different formation channels between the populations.

From Fig. 4.3, we can observe that classifying based on the secondary object differentiates the heavy-mass black holes from stellar-mass black holes better. If the secondary black hole is over $40M_\odot$, which is inside the PISNe mass gap, the primary black hole will also has mass inside the gap. Therefore, both black holes are likely to have similar formation channels that enable the black holes to grow into a heavier mass. The binaries (blue line) involved in the merger tend to have completely different formation channels from the other stellar-mass black holes (orange line). In contrast, we can encounter a binary system with asymmetric mass ratios, so the primary black hole will be classified as heavy mass, while the secondary mass is not high enough. In this case, the two black holes can come from different formation channels, which can largely change the $\mathcal{I}_{\mathrm{BBH}}$ values. $\mathcal{I}_{\mathrm{BBH}}$ are computed with the parameters from both black holes, so binaries with different origins can result in mixed formation channels reflected by $\mathcal{I}_{\mathrm{BBH}}$. Since the heavy-mass BH posterior can contain information from the formation channel of the stellar-mass BH posterior, the curves may not be able to differentiate well even if we use a high threshold mass of $60M_\odot$ to classify. For example, GW190929 has a significantly asymmetric mass ratio, with $m1\_\mathrm{src} \backsim 80.8M_\odot$ and $m2\_\mathrm{src} \backsim 24.1M_\odot$ (L. S. Collaboration and V. Collaboration, 2021). The primary black hole has a large mass inside the PISNe mass gap, which can form from hierarchical mergers or dynamical assembly. However, the secondary black hole has a much smaller mass, which is within a common mass range found in LIGO binaries (Kohler, 2020). The secondary black hole is a typical stellar-mass black hole that may form directly from a massive star (Mirabel, 2017). Using primary mass to classify it will put this BBH merger into the heavy-mass category, while the $\mathcal{I}_{\mathrm{BBH}}$ also has information about the massive star collapse or supernova from the secondary black hole.

Cataloging populations based on secondary compact objects can lead to a more explicit and strict classification. Therefore, we continue using the secondary object to demonstrate the ability of $\mathcal{I}_{\mathrm{BBH}}$ to classify NS and BH in the lower-mass range, which we show in Section 4.3.

4.3 Differentiate Neutron Stars from Black Holes in Lower-Mass Binaries

We showcase $\mathcal{I}_{\rm BBH}$ as a parameter that can be used to differentiate compact objects in the lower mass gap (Bailyn et al., 1998; Özel et al., 2010; Farr et al., 2011). As in Fig. 4.1, we can notice that there are several posteriors distributed in the lower-range of $\mathcal{I}_{\rm BBH}$, which does not overlap with the true astrophysical population (solid black line). These posteriors generally come from events with an unknown secondary compact object. Because $\mathcal{I}_{\rm BBH}$ differentiates formation channels well, the variable should be able to differentiate compact object populations, especially between NS and BH, which have completely different origins.

GWTC-2 & GWTC-3

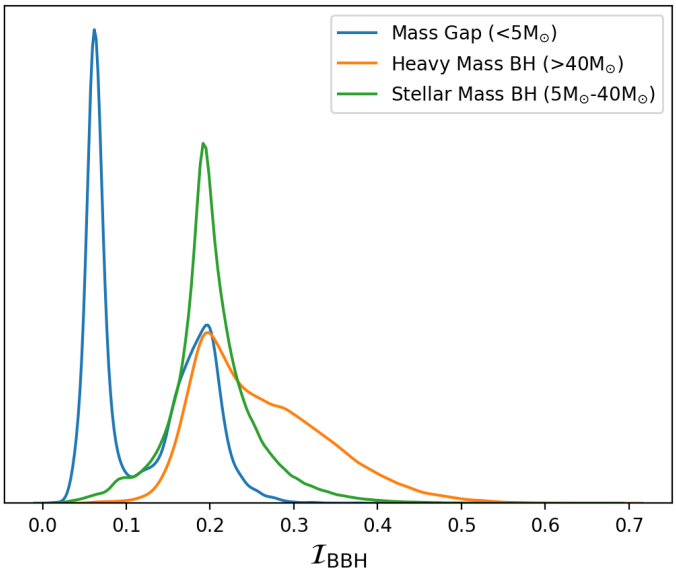

Figure 4.4: $\mathcal{I}_{\rm BBH}$ distribution classified with the secondary compact object $m_{2,\rm src}$. Three events (GW190814 & GW190924 & GW200210) constitute the posterior for the secondary object in the lower mass gap ($\leq 5M_\odot$).

In Fig. 4.4, we categorize GW events from GWTC-2 & GWTC-3 (L. S. Collaboration and V. Collaboration, 2021; L. S. Collaboration, V. Collaboration, and K. Collaboration, 2023) based on the secondary compact object $m_{2,\rm src}$. As explained in the previous section, the heavy-mass black hole posterior (orange) shows a much larger $\mathcal{I}_{\rm BBH}$ range, indicating a different formation channel. Three GW events constitute the posterior of mass gaps (blue curve in Fig. 4.4) – GW190814, GW190924, and GW200210. Note that GW190924 has been confirmed as the least massive BBH merger observed (Psaltis et al., 2021; Alfradique et al., 2023). However, the secondary mass is measured to be $5.0^{+1.4}_{-1.9}\mathrm{M}_\odot$ (L. S. Collaboration and V. Collab-

oration, 2021). The lower bound of the mass posterior extends to the lower mass gap. We will use this least massive BBH as a reference to test the ability of $\mathcal{I}_{\rm BBH}$ to differentiate NS and BH in the lower range. However, GW190814 ($2.59^{+0.08}_{-0.09}\mathrm{M}_{\odot}$) (L. S. Collaboration and V. Collaboration, 2021) and GW200210 ($2.79^{+0.54}_{-0.48}\mathrm{M}_{\odot}$) (L. S. Collaboration, V. Collaboration, and K. Collaboration, 2023) still have unknown secondary objects, which can either be a hypermassive NS, the lightest BH, or another type of compact object within the gap (Zhu et al., 2022).

Differing from the heavier mass and stellar mass black holes, the posterior for the mass gap has two peaks, one at $\mathcal{I}_{\rm BBH} \approx 0.07$ and one at $\mathcal{I}_{\rm BBH} \approx 0.2$, which is similar to the median of the true astrophysical population. The $\mathcal{I}_{\rm BBH}$ range of the larger peak overlaps with the distribution for the stellar-mass black holes by comparing the right peak of the blue distribution and the green distribution in Fig. 4.4. In fact, this larger peak solely comes from GW190924, the lowest mass BBH (L. S. Collaboration and V. Collaboration, 2021), while the smaller sharp peak on the left side comes from GW190814 and GW200210. This left peak has little overlap with the stellar-mass black hole posterior, suggesting that the two events may be NS-BH merger events, which correspond to different formation channels. $\mathcal{I}_{\rm BBH}$ successfully distinguish these two events out.

We then decompose the combined mass gap posterior into individual events in Fig. 4.5. Although $\mathcal{I}_{\rm BBH}$ should only work with BBH merger events, we still compute the distributions of confirmed NS-BH merger events for comparison, including GW191219 and GW200105 (Zhu et al., 2022). We use the SEOBNRv4PHM waveform, which does not incorporate any tidal effects expected in BNS coalescence or NS-BH merger events. Then, we can use the same treatment as BBH mergers and calculate the $\mathcal{I}_{\rm BBH}$ posterior. Generally, NS-BH events have smaller $\mathcal{I}_{\rm BBH}$ values between 0 and 0.15. The posterior always has a sharp spike with a smaller range of $\mathcal{I}_{\rm BBH}$ values compared with BBH merger events. GW190814 has the sharpest peak in these 4 events, spanning a very small range of $\mathcal{I}_{\rm BBH}$, which is very probable and typical for NS-BH merger events. In contrast, GW200210 has a broader range. The upper bound of GW200210 becomes overlapped with the stellar-mass black hole posterior. Although the two events have high similarity (Gayathri et al., 2023), GW190814 has a higher likelihood to have the secondary object as NS than GW200210 based on the $\mathcal{I}_{\rm BBH}$ distributions. The secondary mass for GW190814 is also measured and constrained more precisely than GW200210, making large error bars for the later event (Gayathri et al., 2023). GW200210 has

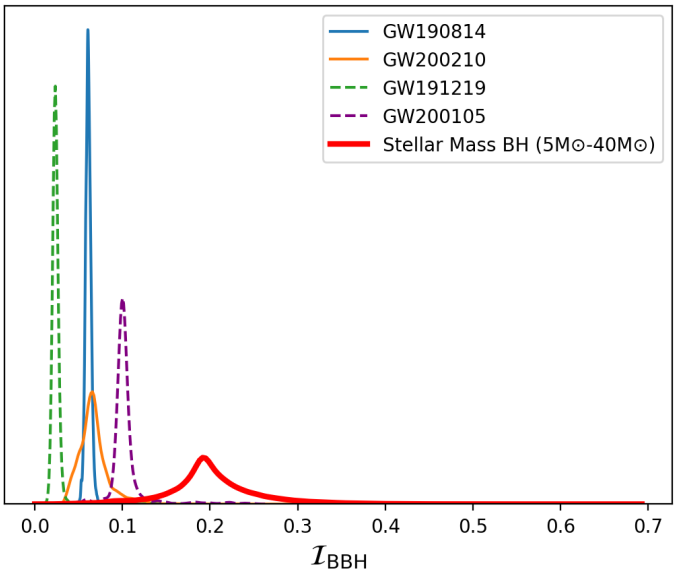

Figure 4.5: $\mathcal{I}_{\rm BBH}$ posteriors of confirmed NS-BH merger events with GW events with unknown secondary objects (solid lines). GW191219 & GW200195, the two NS-BH merger events, are plotted in dotted lines. The bold red line shows the $\mathcal{I}_{\rm BBH}$ posterior of stellar-mass black holes.

a large likelihood as the lightest black hole, which can change the black hole mass distribution if confirmed (Özel et al., 2010).

We have attempted to use $\mathcal{I}_{\rm BBH}$ to classify compact object populations. Although not systematically developed as a pipeline, our model shows some differentiability in the origins and formation channels. Unlike the deformation parameter κ as a constant, $\mathcal{I}_{\rm BBH}$ appears as posteriors for comparison. With more GW events detected by LIGO, we can establish a standard $\mathcal{I}_{\rm BBH}$ posterior for NS-BH binary populations and BBH populations, enabling us to identify the compact objects in the lower mass gap.

New Event from O4: GW230529

The first announced GW event from the 4th observing run of LIGO is GW230529, which is a potential BNS coalescence or NS-BH merger event. The primary compact object has a mass of $3.6^{+0.8}_{-1.3} M_\odot$, which sits in the lower mass gap with 99% confidence interval (Bailyn et al., 1998; Özel et al., 2010; Farr et al., 2011). The secondary compact object will probably be a neutron star with a mass of $1.4^{+0.6}_{-1.2} M_\odot$ (L. S. Collaboration, V. Collaboration, and K. Collaboration, 2024). This event obtains an unknown primary compact object, which we want to identify with $\mathcal{I}_{\rm BBH}$, similar

to the graph in Section 4.3. The $\mathcal{I}_{\rm BBH}$ posterior spans a much broader region than other posteriors in Fig. 4.6. The posterior overlaps with the stellar-mass black hole distribution. Interestingly, this event also displays a bimodality behavior, which is very different from the $\mathcal{I}_{\rm BBH}$ posteriors from BBH or NS-BH merger shown in Fig. 4.5.

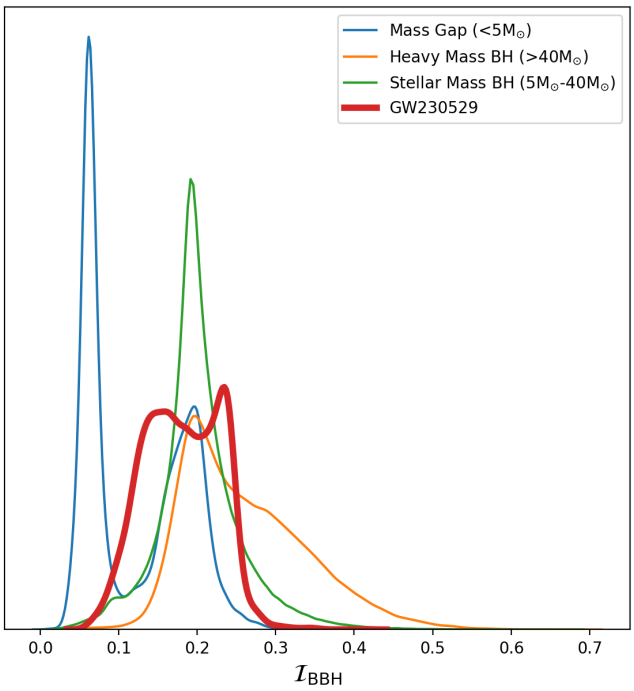

Figure 4.6: $\mathcal{I}_{\rm BBH}$ posteriors of GW230529 with IMRPhenomXHM waveform with reference of $\mathcal{I}_{\rm BBH}$ distributions of compact object populations

This GW event shows a large similarity with GW190426, which is a NS-BH merger event detected in the third observing run (L. S. Collaboration and V. Collaboration, 2021). GW190426 also has a less massive primary object with mass of $5.7^{+3.9}_{-2.3}M_{\odot}$ and a secondary object with mass of $1.5^{+0.8}_{-0.5}M_{\odot}$, which fits into the mass range of neutron stars (Landry and Read, 2021). Both events have a symmetric mass ratio compared with other NS-BH merger events (L. S. Collaboration, V. Collaboration, and K. Collaboration, 2024). This similarity extends to the posteriors of $\mathcal{I}_{\rm BBH}$ too. As seen in Fig. 4.7, both GW190426 and GW230529 show a bimodal $\mathcal{I}_{\rm BBH}$ distribution. By conducting a KS test, the two posteriors have a $\mathcal{D}$ value of 0.26, which does not imply a large difference. The two peaks span a broader range in GW190426 than in GW230529, which can be caused by a more asymmetric mass ratio. The similarity between the two posteriors shows a higher likelihood of GW230529 as a symmetric NS-BH merger event, which supports the conclusion

from the detection paper that the primary object is most likely a black hole (L. S. Collaboration, V. Collaboration, and K. Collaboration, 2024). The mass of the primary object is too heavy to fit into the current neutron star mass distribution. The recent massive pulsar PSR J0514-4002E discovered in a globular cluster has a mass of [2.09, 2.71]$M_{\odot}$, which is one of the most massive neutron stars found (Z.-C. Chen and Liu, 2024). The primary object in GW230529 even exceeds this maximum mass, which is also challenging to fit into NS EoS (Godzieba, Radice, and Bernuzzi, 2021). However, the $\mathcal{I}_{\rm BBH}$ posterior is very different from other NS-BH mergers like GW191219 and GW200105 shown in Fig. 4.5. The large-range posterior also overlaps with the stellar-mass black hole posterior. We cannot rule out the possibility of an exotic compact binary coalescence such as primordial black holes (PBH) dark matter (Huang et al., 2024).

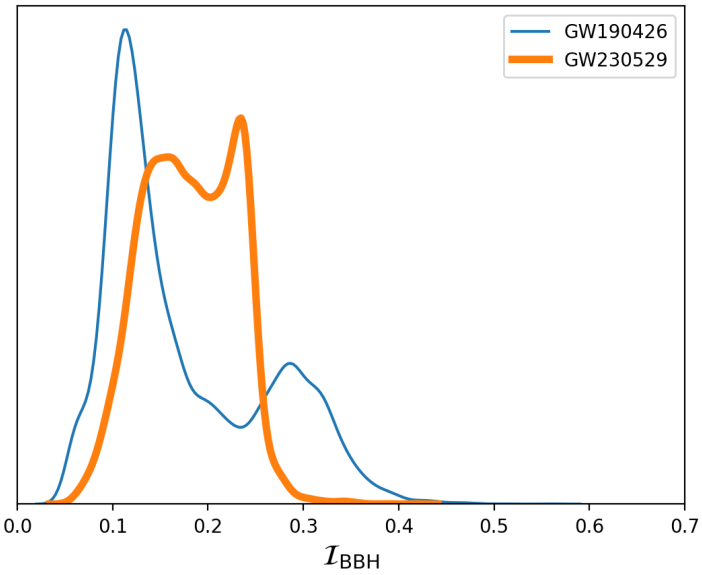

Figure 4.7: The $\mathcal{I}_{\rm BBH}$ posteriors of GW190426 & GW230529

Chapter 5

CONCLUSION

Based on the Hawking Area Theorem, we could calculate the entropy of black holes from mass and spin, which were two parameters measured by LIGO. With this theorem, we derived a variable $\mathcal{I}_{\rm BBH}$ that measured the efficiency of entropy transfer during BBH mergers. To apply $\mathcal{I}_{\rm BBH}$ on GW data, we coded and constructed a framework that imposes thermodynamical constraints derived from general relativity and quasi-circular hypothesis. When there was an independent measurement of the ringdown phase (QNM), this framework operated as an IMR consistency test, which gives us new astrophysical insights. By applying the framework to 10 of the heaviest BBH mergers detected by LVK with both the IMR analysis and independent ringdown measurement, we found new astrophysical insights into the formation channels for GW190521 and GW191109, two of the heaviest confirmed binary black hole merger events. Meanwhile, we independently used entropy to prove the existence of black holes inside the PISNe mass gap.

We systematically investigated the consistency between the phenomenological waveform and the ringdown model. The optimal filtering cut ρ was 75% for both the theoretical limit and uniform prior, which also disabled any faulty astrophysical insights. With this filtering cut, we tested and discovered $\rm Kerr_{221}$ as the most consistent ringdown model. This finding supported the claim that the ringdown stage may start early in the merger stage. In contrast, $\rm Kerr_{HM}$ showed the lowest consistency, suggesting the absence of these high-order modes in symmetric GW events. Compared with QNMs, waveforms did not largely affect the consistency between posteriors. NRSur7dq4 waveform displayed the highest consistency with the ringdown models, indicating the importance of numerical relativity simulations to waveform constructions.

For events without the QNM measurement due to the low SNR of ringdown, we utilized the post-merger conditions fitted from the IMR waveform, which allowed us to compute the $\mathcal{I}_{\rm BBH}$ for all GW events. We derived the astrophysical distribution of $\mathcal{I}_{\rm BBH}$, which shows high differentiability. Therefore, we saw the potential of $\mathcal{I}_{\rm BBH}$ to differentiate formation channels and classify compact binary populations. Based on the mass of the secondary black hole, we separated heavy-mass black holes from

stellar-mass black holes, demonstrating that they correspond to different formation channels. Similarly, we applied the $\mathcal{I}_{\rm BBH}$ value to the lower-mass gap to identify the compact object. We showed some preliminary results to differentiate NS-BH from BBH merger events. With $\mathcal{I}_{\rm BBH}$ posteriors, we demonstrated the high probability of the newest LIGO discovery GW230529 as a NS-BH merger event.

BIBLIOGRAPHY

Abbott, B. P. et al. (Feb. 2016a). "Observation of Gravitational Waves from a Binary Black Hole Merger". In: *Phys. Rev. Lett.* 116 (6), p. 061102. DOI: 10.1103/PhysRevLett.116.061102. URL: https://link.aps.org/doi/10.1103/PhysRevLett.116.061102.

– (2016b). "Properties of the Binary Black Hole Merger GW150914". In: *Phys. Rev. Lett.* 116.24, p. 241102. DOI: 10.1103/PhysRevLett.116.241102. arXiv: 1602.03840 [gr-qc].

– (2019). "Properties of the binary neutron star merger GW170817". In: *Phys. Rev. X* 9.1, p. 011001. DOI: 10.1103/PhysRevX.9.011001. arXiv: 1805.11579 [gr-qc].

Abbott, R. et al. (2020a). "GW190412: Observation of a Binary-Black-Hole Coalescence with Asymmetric Masses". In: *Phys. Rev. D* 102.4, p. 043015. DOI: 10.1103/PhysRevD.102.043015. arXiv: 2004.08342 [astro-ph.HE].

– (2020b). "GW190521: A Binary Black Hole Merger with a Total Mass of $150M_{\odot}$". In: *Phys. Rev. Lett.* 125.10, p. 101102. DOI: 10.1103/PhysRevLett.125.101102. arXiv: 2009.01075 [gr-qc].

– (2020c). "GW190814: Gravitational Waves from the Coalescence of a 23 Solar Mass Black Hole with a 2.6 Solar Mass Compact Object". In: *Astrophys. J. Lett.* 896.2, p. L44. DOI: 10.3847/2041-8213/ab960f. arXiv: 2006.12611 [astro-ph.HE].

– (2021a). "Observation of Gravitational Waves from Two Neutron Star"–Black Hole Coalescences". In: *Astrophys. J. Lett.* 915.1, p. L5. DOI: 10.3847/2041-8213/ac082e. arXiv: 2106.15163 [astro-ph.HE].

– (2021b). "Tests of general relativity with binary black holes from the second LIGO-Virgo gravitational-wave transient catalog". In: *Phys. Rev. D* 103.12, p. 122002. DOI: 10.1103/PhysRevD.103.122002. arXiv: 2010.14529 [gr-qc].

– (Dec. 2021c). "Tests of General Relativity with GWTC-3". In: arXiv: 2112.06861 [gr-qc].

Alfradique, V. et al. (2023). *A dark siren measurement of the Hubble constant using gravitational wave events from the first three LIGO/Virgo observing runs and DELVE*. arXiv: 2310.13695 [astro-ph.CO].

Antonelli, Andrea et al. (2023). *Classifying the generation and formation channels of individual LIGO-Virgo-KAGRA observations from dynamically formed binaries*. arXiv: 2306.11088 [gr-qc].

Bailyn, Charles D. et al. (May 1998). "The Mass Distribution of Stellar Black Holes". In: *The Astrophysical Journal* 499.1, pp. 367–374. ISSN: 1538-4357. DOI: 10.1086/305614. URL: http://dx.doi.org/10.1086/305614.

Bardeen, James M., B. Carter, and S. W. Hawking (1973). "The Four laws of black hole mechanics". In: *Commun. Math. Phys.* 31, pp. 161–170. DOI: 10.1007/BF01645742.

Bekenstein, Jacob D. (Apr. 1973). "Black Holes and Entropy". In: *Phys. Rev. D* 7 (8), pp. 2333–2346. DOI: 10.1103/PhysRevD.7.2333. URL: https://link.aps.org/doi/10.1103/PhysRevD.7.2333.

Berti, Emanuele, Vitor Cardoso, and Andrei O Starinets (July 2009). "Quasinormal modes of black holes and black branes". In: *Classical and Quantum Gravity* 26.16, p. 163001. ISSN: 1361-6382. DOI: 10.1088/0264-9381/26/16/163001. URL: http://dx.doi.org/10.1088/0264-9381/26/16/163001.

Capano, Collin D. et al. (2023). *Statistical validation of the detection of a subdominant quasi-normal mode in GW190521*. arXiv: 2209.00640 [gr-qc].

Carullo, Gregorio, Walter Del Pozzo, and John Veitch (July 2023). *pyRing: a time-domain ringdown analysis python package*. git.ligo.org/lscsoft/pyring. Version 2.3.0. DOI: 10.5281/zenodo.8165508. URL: https://doi.org/10.5281/zenodo.8165508.

Chen, Zu-Cheng and Lang Liu (2024). *Is PSR J0514−4002E in a PBH-NS binary?* arXiv: 2401.12889 [astro-ph.HE].

Chen, Hsin-Yu et al. (Jan. 2017). "Observational Selection Effects with Ground-based Gravitational Wave Detectors". In: 835.1, 31, p. 31. DOI: 10.3847/1538-4357/835/1/31. arXiv: 1608.00164 [astro-ph.HE].

Collaboration, LIGO Scientific and Virgo Collaboration (June 2021). "GWTC-2: Compact Binary Coalescences Observed by LIGO and Virgo during the First Half of the Third Observing Run". In: *Phys. Rev. X* 11 (2), p. 021053. DOI: 10.1103/PhysRevX.11.021053. URL: https://link.aps.org/doi/10.1103/PhysRevX.11.021053.

Collaboration, LIGO Scientific, Virgo Collaboration, and KAGRA Collaboration (Dec. 2023). "GWTC-3: Compact Binary Coalescences Observed by LIGO and Virgo during the Second Part of the Third Observing Run". In: *Phys. Rev. X* 13 (4), p. 041039. DOI: 10.1103/PhysRevX.13.041039. URL: https://link.aps.org/doi/10.1103/PhysRevX.13.041039.

– (2024). *Observation of Gravitational Waves from the Coalescence of a* 2.5 – 4.5 $M_\odot$ *Compact Object and a Neutron Star*. arXiv: 2404.04248 [astro-ph.HE].

Correia, Alex and Collin D. Capano (2023). *Sky marginalization in black hole spectroscopy and tests of the area theorem*. arXiv: 2312.15146 [gr-qc].

Dichiara, S. et al. (Dec. 2021). "Constraints on the Electromagnetic Counterpart of the Neutron-star–Black-hole Merger GW200115". In: *The Astrophysical Journal Letters* 923.2, p. L32. ISSN: 2041-8213. DOI: 10.3847/2041-8213/ac4259. URL: http://dx.doi.org/10.3847/2041-8213/ac4259.

Farmer, R. et al. (Dec. 2019). "Mind the Gap: The Location of the Lower Edge of the Pair-instability Supernova Black Hole Mass Gap". In: *The Astrophysical Journal* 887.1, p. 53. ISSN: 1538-4357. DOI: 10.3847/1538-4357/ab518b. URL: http://dx.doi.org/10.3847/1538-4357/ab518b.

Farr, Will M. et al. (Oct. 2011). "THE MASS DISTRIBUTION OF STELLAR-MASS BLACK HOLES". In: *The Astrophysical Journal* 741.2, p. 103. ISSN: 1538-4357. DOI: 10.1088/0004-637x/741/2/103. URL: http://dx.doi.org/10.1088/0004-637X/741/2/103.

Finch, Eliot and Christopher J. Moore (Apr. 2021). "Modeling the ringdown from precessing black hole binaries". In: *Physical Review D* 103.8. ISSN: 2470-0029. DOI: 10.1103/physrevd.103.084048. URL: http://dx.doi.org/10.1103/PhysRevD.103.084048.

Fishbach, Maya and Daniel E. Holz (Nov. 2020). "Minding the Gap: GW190521 as a Straddling Binary". In: *The Astrophysical Journal Letters* 904.2, p. L26. ISSN: 2041-8213. DOI: 10.3847/2041-8213/abc827. URL: http://dx.doi.org/10.3847/2041-8213/abc827.

Flanagan, Éanna É. and Scott A. Hughes (Apr. 1998). "Measuring gravitational waves from binary black hole coalescences. I. Signal to noise for inspiral, merger, and ringdown". In: *Physical Review D* 57.8, pp. 4535–4565. ISSN: 1089-4918. DOI: 10.1103/physrevd.57.4535. URL: http://dx.doi.org/10.1103/PhysRevD.57.4535.

Forteza, Xisco Jiménez and Pierre Mourier (Dec. 2021). "High-overtone fits to numerical relativity ringdowns: Beyond the dismissed n=8 special tone". In: *Physical Review D* 104.12. ISSN: 2470-0029. DOI: 10.1103/physrevd.104.124072. URL: http://dx.doi.org/10.1103/PhysRevD.104.124072.

Gayathri, V. et al. (2023). *Do gravitational wave observations in the lower mass gap favor a hierarchical triple origin?* arXiv: 2307.09097 [astro-ph.HE].

Ghosh, Abhirup, Richard Brito, and Alessandra Buonanno (June 2021). "Constraints on quasinormal-mode frequencies with LIGO-Virgo binary–black-hole observations". In: *Physical Review D* 103.12. ISSN: 2470-0029. DOI: 10.1103/physrevd.103.124041. URL: http://dx.doi.org/10.1103/PhysRevD.103.124041.

Ghosh, Abhirup, Archisman Ghosh, et al. (July 2016). "Testing general relativity using golden black-hole binaries". In: *Physical Review D* 94.2. ISSN: 2470-0029. DOI: 10.1103/physrevd.94.021101. URL: http://dx.doi.org/10.1103/PhysRevD.94.021101.

Godzieba, Daniel A., David Radice, and Sebastiano Bernuzzi (Feb. 2021). "On the Maximum Mass of Neutron Stars and GW190814". In: *The Astrophysical Journal* 908.2, p. 122. ISSN: 1538-4357. DOI: 10.3847/1538-4357/abd4dd. URL: http://dx.doi.org/10.3847/1538-4357/abd4dd.

Greene, Jenny E., Jay Strader, and Luis C. Ho (Aug. 2020). "Intermediate-Mass Black Holes". In: *Annual Review of Astronomy and Astrophysics* 58.1, pp. 257–312. ISSN: 1545-4282. DOI: 10.1146/annurev-astro-032620-021835. URL: http://dx.doi.org/10.1146/annurev-astro-032620-021835.

Hawking, S. W. (May 1971). "Gravitational Radiation from Colliding Black Holes". In: *Phys. Rev. Lett.* 26 (21), pp. 1344–1346. DOI: 10.1103/PhysRevLett.26.1344. URL: https://link.aps.org/doi/10.1103/PhysRevLett.26.1344.

Hu, Patrick et al. (2021). *Thermodynamics to infer the astrophysics of binary black hole mergers*. arXiv: 2112.06856 [gr-qc].

Huang, Qing-Guo et al. (2024). *GW230529_181500: A Potential Primordial Binary Black Hole Merger in the Mass Gap*. arXiv: 2404.05691 [gr-qc].

Isi, Maximiliano et al. (Sept. 2019). "Testing the No-Hair Theorem with GW150914". In: *Physical Review Letters* 123.11. ISSN: 1079-7114. DOI: 10.1103/physrevlett.123.111102. URL: http://dx.doi.org/10.1103/PhysRevLett.123.111102.

Islam, Tousif et al. (2023). *Analysis of GWTC-3 with fully precessing numerical relativity surrogate models*. arXiv: 2309.14473 [gr-qc].

Kohler, Susanna (Sept. 2020). *LIGO/Virgo' Newest Merger Defies Mass Expectations*. AAS Nova Highlight, 02 Sep 2020, id.6972.

Landry, Philippe and Jocelyn S. Read (Nov. 2021). "The Mass Distribution of Neutron Stars in Gravitational-wave Binaries". In: *The Astrophysical Journal Letters* 921.2, p. L25. ISSN: 2041-8213. DOI: 10.3847/2041-8213/ac2f3e. URL: http://dx.doi.org/10.3847/2041-8213/ac2f3e.

Ma, Sizheng et al. (Oct. 2022). "Quasinormal-mode filters: A new approach to analyze the gravitational-wave ringdown of binary black-hole mergers". In: 106.8, 084036, p. 084036. DOI: 10.1103/PhysRevD.106.084036. arXiv: 2207.10870 [gr-qc].

Marchant, Pablo and Takashi J. Moriya (Aug. 2020). "The impact of stellar rotation on the black hole mass-gap from pair-instability supernovae". In: *Astronomy & Astrophysics* 640, p. L18. ISSN: 1432-0746. DOI: 10.1051/0004-6361/202038902. URL: http://dx.doi.org/10.1051/0004-6361/202038902.

Mirabel, Félix (Aug. 2017). "The formation of stellar black holes". In: 78, pp. 1–15. DOI: 10.1016/j.newar.2017.04.002.

O'Brien, B. et al. (Oct. 2021). "Detection of LIGO-Virgo binary black holes in the pair-instability mass gap". In: *Physical Review D* 104.8. ISSN: 2470-0029. DOI: 10.1103/physrevd.104.082003. URL: http://dx.doi.org/10.1103/PhysRevD.104.082003.

Özel, Feryal et al. (Dec. 2010). "THE BLACK HOLE MASS DISTRIBUTION IN THE GALAXY". In: *The Astrophysical Journal* 725.2, pp. 1918–1927. ISSN: 1538-4357. DOI: 10.1088/0004-637x/725/2/1918. URL: http://dx.doi.org/10.1088/0004-637X/725/2/1918.

Pan, Yi et al. (Apr. 2014). "Inspiral-merger-ringdown waveforms of spinning, precessing black-hole binaries in the effective-one-body formalism". In: *Physical Review D* 89.8. ISSN: 1550-2368. DOI: 10.1103/physrevd.89.084006. URL: http://dx.doi.org/10.1103/PhysRevD.89.084006.

Popovic, Marko (2017). *Researchers in an Entropy Wonderland: A Review of the Entropy Concept*. arXiv: 1711.07326 [physics.chem-ph].

Psaltis, Dimitrios et al. (May 2021). "Probing the black hole metric: Black hole shadows and binary black-hole inspirals". In: *Physical Review D* 103.10. ISSN: 2470-0029. DOI: 10.1103/physrevd.103.104036. URL: http://dx.doi.org/10.1103/PhysRevD.103.104036.

Romero-Shaw, Isobel, Paul D. Lasky, and Eric Thrane (Dec. 2022). "Four Eccentric Mergers Increase the Evidence that LIGO–Virgo–KAGRA's Binary Black Holes Form Dynamically". In: *The Astrophysical Journal* 940.2, p. 171. ISSN: 1538-4357. DOI: 10.3847/1538-4357/ac9798. URL: http://dx.doi.org/10.3847/1538-4357/ac9798.

Sá, L. M. de et al. (Dec. 2022). "Quantifying the Evidence Against a Mass Gap between Black Holes and Neutron Stars". In: *The Astrophysical Journal* 941.2, p. 130. ISSN: 1538-4357. DOI: 10.3847/1538-4357/aca076. URL: http://dx.doi.org/10.3847/1538-4357/aca076.

Safarzadeh, Mohammadtaher, Will M. Farr, and Enrico Ramirez-Ruiz (May 2020). "A Trend in the Effective Spin Distribution of LIGO Binary Black Holes with Mass". In: *The Astrophysical Journal* 894.2, p. 129. ISSN: 1538-4357. DOI: 10.3847/1538-4357/ab80be. URL: http://dx.doi.org/10.3847/1538-4357/ab80be.

Setyawati, Yoshinta and Frank Ohme (June 2021). "Adding eccentricity to quasicircular binary-black-hole waveform models". In: *Physical Review D* 103.12. ISSN: 2470-0029. DOI: 10.1103/physrevd.103.124011. URL: http://dx.doi.org/10.1103/PhysRevD.103.124011.

Talbot, Colm and Eric Thrane (Apr. 2018). "Measuring the Binary Black Hole Mass Spectrum with an Astrophysically Motivated Parameterization". In: *The Astrophysical Journal* 856.2, p. 173. DOI: 10.3847/1538-4357/aab34c. URL: https://dx.doi.org/10.3847/1538-4357/aab34c.

Thorne, Kip S. (Apr. 1980). "Multipole expansions of gravitational radiation". In: *Reviews of Modern Physics* 52.2, pp. 299–340. DOI: 10.1103/RevModPhys.52.299.

Varma, Vijay, Scott E. Field, et al. (Mar. 2019). "Surrogate model of hybridized numerical relativity binary black hole waveforms". In: *Physical Review D* 99.6. ISSN: 2470-0029. DOI: 10.1103/physrevd.99.064045. URL: http://dx.doi.org/10.1103/PhysRevD.99.064045.

Varma, Vijay, Davide Gerosa, et al. (Jan. 2019). "High-Accuracy Mass, Spin, and Recoil Predictions of Generic Black-Hole Merger Remnants". In: *Physical Review Letters* 122.1. ISSN: 1079-7114. DOI: 10.1103/physrevlett.122.011101. URL: http://dx.doi.org/10.1103/PhysRevLett.122.011101.

Wang, Yi-Fan et al. (Oct. 2022). "Tests of gravitational-wave birefringence with the open gravitational-wave catalog". In: *Physical Review D* 106.8. ISSN: 2470-0029. DOI: 10.1103/physrevd.106.084005. URL: http://dx.doi.org/10.1103/PhysRevD.106.084005.

Woosley, S. E. and Alexander Heger (May 2021). "The Pair-instability Mass Gap for Black Holes". In: *The Astrophysical Journal Letters* 912.2, p. L31. ISSN: 2041-8213. DOI: 10.3847/2041-8213/abf2c4. URL: http://dx.doi.org/10.3847/2041-8213/abf2c4.

Zevin, Michael et al. (Aug. 2020). "Exploring the Lower Mass Gap and Unequal Mass Regime in Compact Binary Evolution". In: *The Astrophysical Journal Letters* 899.1, p. L1. ISSN: 2041-8213. DOI: 10.3847/2041-8213/aba74e. URL: http://dx.doi.org/10.3847/2041-8213/aba74e.

Zhang, Rachel C. et al. (2023). *On the Likely Dynamical Origin of GW191109 and of Binary Black Hole Mergers with Negative Effective Spin*. arXiv: 2302.07284 [astro-ph.HE].

Zhu, Jin-Ping et al. (Apr. 2022). "Population Properties of Gravitational-wave Neutron Star–Black Hole Mergers". In: *The Astrophysical Journal* 928.2, p. 167. ISSN: 1538-4357. DOI: 10.3847/1538-4357/ac540c. URL: http://dx.doi.org/10.3847/1538-4357/ac540c.